INCONSISTENCIES IN THE WEATHER RESEARCH AND FORECASTING MODEL OF THE MARINE BOUNDARY LAYER ALONG THE COAST OF CALIFORNIA

By

© 2017

Andrew M. Fisher

Submitted to the graduate degree program in Geography and Atmospheric Science and the Graduate Faculty of the University of Kansas in partial fulfillment of the requirements for the degree of Master of Science.

_____

David Rahn
Chairperson

_____

David Mechem

_____

David Braaten

Date Defended: May 18, 2017

The Thesis Committee for Andrew M. Fisher

certifies that this is the approved version of the following thesis:

INCONSISTENCIES IN THE WEATHER RESEARCH AND FORECASTING MODEL OF THE MARINE BOUNDARY LAYER ALONG THE COAST OF CALIFORNIA

_____

David Rahn

Chairperson

Date Approved: May 18, 2017

ABSTRACT

The late spring and summer low-level wind field along the California coast is primarily controlled by the pressure gradient between the Pacific high and the thermal low over the desert southwest. Strong northwesterly winds within the marine boundary layer (MBL) are common and the flow is often described as a two-layer shallow water hydraulic system, capped above by subsidence and bounded laterally by high coastal topography. Hydraulic features such as an expansion fan can occur near major coastal headlands. Numerical simulations using the Weather Research and Forecasting (WRF) modeling system were conducted over a two-month period and compared to observations from several buoy stations and aircraft measurements from the Precision Atmospheric Marine Boundary Layer Experiment (PreAMBLE). Model performance of the atmospheric adjustment near the Point Arguello and Point Conception (PAPC) headlands and into the Santa Barbara Channel (SBC) is assessed. Substantial inconsistencies are revealed, especially in the SBC. The strength of the synoptic forcing impacts model performance upstream of PAPC. The model maintains stronger winds than observed under weak forcing regimes, inadequately representing periods of wind relaxation. The large-scale forcing has minimal impact on the flow in the SBC, where poor modeling of the MBL characteristics exists throughout the entire period. Similar results are found in the coarser North American Mesoscale (NAM) model. In general, WRF overestimates the wind speed around PAPC and the expansion fan extends too far into the SBC. Previous conceptual models were based on similar flawed model results and limited observations. PreAMBLE measurements reveal a more complex lower atmosphere in the SBC than the simulations can represent. Mischaracterization of surface wind stress in the SBC has implications for forcing ocean models with WRF. Understanding model biases of the vertical profile of temperature and humidity are also critical to several national defense agencies with interests in atmospheric refractivity conditions and its impact on their operations.

ACKNOWLEDGEMENTS

First and foremost, I would like to express my sincere gratitude to my advisor Dr. David Rahn for the endless support he has given me as I worked to obtain this degree. I am truly fortunate to have had the opportunity to work with him on this interesting project and could not have asked for a better advisor. I would also like to thank my committee members: Dr. David Mechem and Dr. David Braaten for their insightful ideas and involvement in my research. Without their support and guidance, completing this thesis would not be possible. For this, I thank all of you.

Besides my committee, a special thanks also goes to the entire faculty in the Department of Geography and Atmospheric Science at the University of Kansas for their instruction and collaboration, both in and out of the classroom. To all my fellow graduate students, thank you for making daily work at the office enjoyable during the last few years. Good luck to all of you and your future endeavors.

In addition to everyone at Kansas, I would like to express my sincere gratitude to my family for supporting me throughout this journey, especially to those that I have lost during this time.

To my late Pop, Boniface Damiano: Ever since I was in grade school, your enthusiasm for learning and support of higher education has molded me into the man I have become today. I will carry your life lessons and stories with me for the rest of my life. I miss you dearly.

To my late grandmother, Ina Fisher: Your everlasting love and support gave me the confidence to keep pushing forward, even when I was so far from home. You were always so proud of my achievements, and I wish you were here to see me complete my degree as I begin the next chapter in my life.

A very special thanks goes to my grandmother, Dr. Leonora Damiano, for giving me the ambition to pursue this degree. As a scholar and accomplished educator yourself, you have been a role model and inspiration. You have instilled in me to value education and to be a life-long learner.

And of course, I thank my parents for their love and support throughout my entire life. I am so grateful to have you both and extremely fortunate for the foundation you have laid for me to become who I am today. To my older siblings, Jeff and Lauren, you both are role models to me. I look up to your success, even though I have surpassed both of you in many respects!

Last but not least, I could not have done this without the support of all my friends back in New Jersey. I thank all of you for being there for me, especially through the more difficult times in recent years.

TABLE OF CONTENTS

LIST OF FIGURES

LIST OF TABLES

Chapter One
Introduction

1.1) Introduction

Along the west coast of the United States during the spring and summer months, the mean synoptic-scale atmospheric conditions support northwesterly wind along the coast. The dominant pattern is a subtropical anticyclone centered ~1000 km offshore and a thermal low over the Desert Southwest (Beardsley et al. 1987; Burk and Thompson 1996; Dorman and Koračin 2008; Parish et al. 2014). The strong low-level horizontal pressure gradient force (PGF) between the Pacific high and thermal low drives the coastal wind. Subsidence associated with the subtropical branch of the Hadley circulation maintains a large temperature inversion between the moist, cool air within the marine boundary layer (MBL) and the dry, warm subsiding air above (Beardsley et al. 1987). MBL depth is typically as low as 100 m adjacent to the coast, and as high as 600 m, at approximately 100 km offshore (Pomeroy and Parish 2001). Since the inversion height slopes down towards the coast, there is a large horizontal temperature gradient and thermal wind that is associated with the jet maximum (Beardsley et al. 1987; Lester 1985; Gerber et al. 1989; Parish 2000). The low-level jet (LLJ) is at maximum intensity near the top of the MBL, and it is primarily forced by strong baroclinicity (Burk and Thompson 1996).

The lower atmosphere near the coast is typically thought of in terms of a two-layer shallow water system that is bounded by a lateral boundary since the depth of the MBL is normally lower than the adjacent topography. Large local adjustments of the along-shore flow to convex or concave changes in the coastline can occur and greatly impact the MBL. Modeling and observations of the local flow adjustment to changes of the coastline has revealed that to a first order the flow behaves similar to open channel engineering applications, or “hydraulic” flow. In geophysics, hydraulic flow refers to wind or current systems that behave like the flow in spillways, weirs, aqueducts, and similar systems.

The Precision Atmospheric Marine Boundary Layer Experiment (PreAMBLE) measured the lower atmosphere in southern California to investigate the flow response to the most extreme bend in the coastline near Point Conception (Fig. 1.1). Several flights

were conducted throughout May and June 2012 with the University of Wyoming King Air research aircraft, and those measurements are used to evaluate the dynamics of the coastal jet within the MBL. These rare aircraft measurements are also compared to model output, which forms the basis for much of this work.

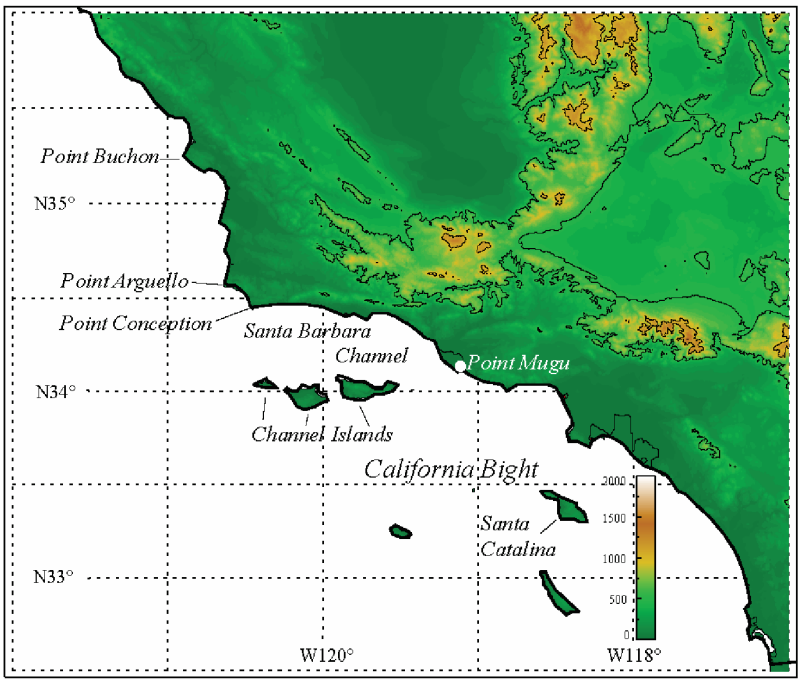

Fig. 1.1: Map of the PreAMBLE study area with key features identified and topography height contoured every 500 m and color filled.

The coastal environment is a demanding test for numerical weather prediction models. Complex interactions in the coastal margin between synoptic and mesoscale processes confound model solutions, posing a challenge to weather forecasters in coastal regions (Ranjha et al. 2016). Understanding model bias along the west coast is important for many applications including wind energy forecasting (e.g., Shimada and Ohsawa 2011; Carvalho et al. 2012; Carvalho et al. 2014; Chang et al. 2015; Mattar and Borvarán 2016), understanding ocean upwelling processes near the coast (e.g., Enriquez and Friehe 1996; Pickett and Paduan 2003; Renault et al. 2009; Garreaud et al. 2011; Seo et al. 2012; Bravo et al. 2016), forcing ocean models with modeled surface wind (e.g., Capet et al. 2004; Jin et al. 2009; Perlin et al. 2011; Renault et al. 2012), and attribution of anomalous

electromagnetic wave propagation (e.g., Burk and Thompson 1997; Burk et al. 1999; Haack and Burk 2001; Brooks et al. 1999; Haack et al. 2010; Thompson and Haack 2011).

1.2) Research Questions and Methodologies

After a preliminary comparison of aircraft observations with operational models and numerical simulations of a few case studies, notable model deficiencies in this complex coastal environment were exposed. Conceptual models of the region have been at least partially based on model results, so it is necessary to assess the inconsistencies between the observations and numerical simulations, which in turn impacts the interpretation of the lower atmosphere in this region. Since just a few simulated case studies may not be representative, the entire period during PreAMBLE is simulated and compared to all available observations. Specifically, the Weather Research and Forecasting (WRF) modeling system is used. Prior to PreAMBLE, there were only limited aircraft observations off the coast of Point Conception (Edinger and Wurtele 1972), which makes the new data obtained during PreAMBLE particularly valuable.

The fundamental purpose of this study is to evaluate numerical model performance (WRF) in the coastal region of southern California (Fig. 1.1). Buoy data are the traditional metric used to test model performance, and the lack of upper air observations in the region has precluded any way to connect surface biases with conditions aloft. Aircraft measurements during PreAMBLE are used to extend the analysis above the surface. Model inconsistencies are linked to environmental and synoptic conditions to identify processes that could most likely contribute to model errors. Three main research questions, followed by a hypothesis, direct the analysis.

(1) Where are model inconsistencies the greatest along the coast of southern California?
Largest differences between the model and observations will occur between Point Arguello and the western Santa Barbara Channel where the largest hydraulic response occurs.

The background synoptic flow should be fairly well-represented. The most complex forcing along the coast occurs due to topographical heterogeneities impacting the lower

atmosphere (Skyllingstad et al. 2001). It will likely be more difficult to simulate the local flow modification due to the considerable changes of the coastline downstream of Point Conception and into the Santa Barbara Channel (SBC). The modification of the low-level flow is important because it changes the wind stress near the coast, which impacts ocean upwelling. Data from several buoys and coastal stations will be compared to model output to determine the location where observations deviate from the model the most. Observational data are from the National Oceanic and Atmospheric Administration's (NOAA) National Data Buoy Center (NDBC, http://www.ndbc.noaa.gov).

(2) Are model errors larger under certain synoptic conditions?

Large-scale pressure features drive the coastal low-level dynamics and influence MBL response near coastal topography. Under weak synoptic forcing the more complex mesoscale features will lead to greater differences between the model and observations.

The synoptic pattern is the dominant control on the coastal winds. If the synoptic forcing is strong, the coastal wind within the model simulation is more likely to correspond well with observations. During weak synoptic forcing, poor performance of numerical simulations along the coast could be due to the difficulty in representing mesoscale forcing. In this scenario, more model error is expected because of poorly resolved or represented mesoscale responses that become more important. Minor adjustments to the MBL structure can cause significant changes to related features such as the marine layer stratus (Koračin et al. 2001). The strength of synoptic forcing will be based on the surface wind speed and classified as strong, moderate, or weak. The mean daily wind speed from several buoys and coastal stations along the coast will be used to define the categories and use the criteria defined in the synoptic forcing metric. These events are compared and tested for significant difference in errors.

(3) What are the implications associated with poor model performance?

Observations indicate complex/subtle structures in the Santa Barbara Channel, but these are not represented in WRF and lead to errors in other applications.

Case studies of the observations revealed complex structures from aircraft observations in the lower atmosphere in the SBC, but preliminary comparisons to model output indicate that these are not well-represented in the simulations. A sufficient vertical and horizontal resolution is necessary to represent subtle features in the model. Since these layers are thin, the grid spacing must be sufficiently small to represent the fine-scale features and sharp transitions present in the aircraft observations. Features such as large temperature and moisture gradients at the top of the MBL can greatly impact the propagation of electromagnetic radiation, which can have significant implications to the path and intensity of microwave radar energy and communication signals (Burk and Thompson 1997). To examine the model's ability to capture fine-scale vertical structure of the MBL, WRF simulations are compared with aircraft observations from the PreAMBLE. The atmospheric refractivity is investigated in more depth by comparing the model to observations as a case study of two events during the field campaign.

1.3) Review of the Coastal Environment

The North Pacific high strengthens and moves northward during spring and is the dominant feature until autumn (Fig. 1.2). Strong equatorward surface wind along the coast induces offshore Ekman transport of surface water that is replaced from below by the cool, nutrient-rich water, greatly influencing bioproductivity. Wind stress curl also contributes to upwelling (e.g., Koračin et al. 2004), and only more recently have higher resolution data sets and simulations have been able to examine the curl in adequate detail (e.g., Bravo et al. 2016). The LLJ is weakest in the early morning, and it is strongest during the late afternoon and early evening. The diurnal wind maximum lags the low-level maximum baroclinicity as it undergoes geostrophic adjustment, and the timing is influenced by both the diurnal and inertial periods (Burk and Thompson 1996; Ranjha et al. 2016).

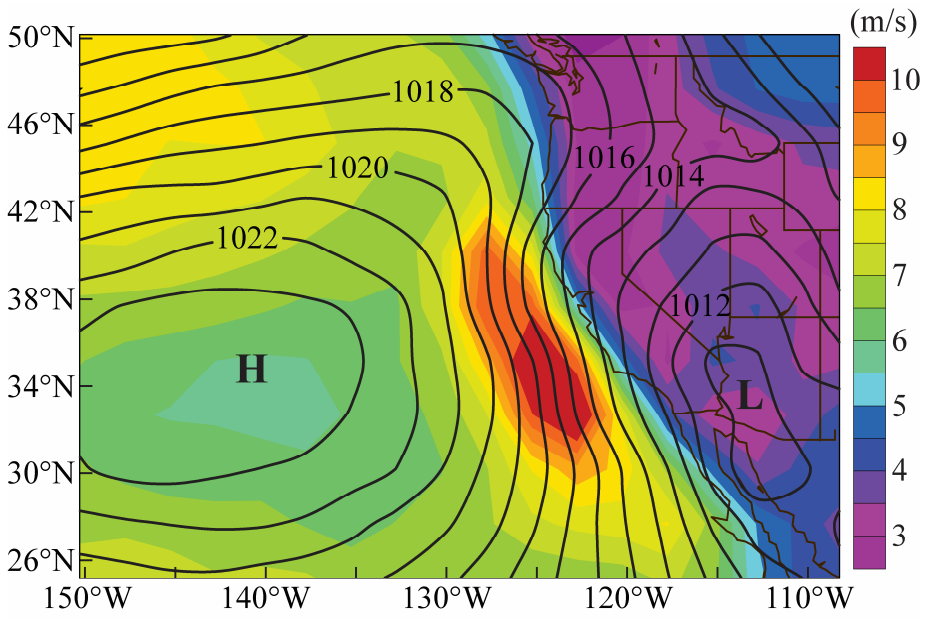

Fig. 1.2: Composite of the mean sea level pressure (contoured every 1 hPa) and the surface wind speed (color filled every 0.5 m s^{-1}) during the months of May and June from 2002-2012. Data are obtained from the NCEP/NCAR Reanalysis monthly/seasonal composites product (http://www.esrl.noaa.gov/psd/data/composites). The position of the Pacific high and thermal low are illustrated as H and L, respectively.

Mesoscale variability of the coastal wind and the MBL depth is largely driven by the interaction between the persistent northwesterly flow contained in the MBL and the coastal topography (Dorman 1985; Dorman et al. 1999; Dorman and Koračin 2008; Edwards et al. 2001; Haack et al. 2001; Skyllingstad et al. 2001). Wind speed maxima are found in the lee of points or capes along the coastline (Dorman and Koračin 2008). In these regions, local LLJ enhancement directly impacts SST variability (Ranjha et al. 2016). Since the coastal topography is generally higher than the MBL depth, the coastal flow is confined by this geographic lateral boundary (Haack et al. 2001; Rahn et al. 2013; Ranjha et al. 2016). Thus, the atmospheric low-level flow acts as an incompressible fluid that can be approximated by a two-layer shallow water model (Winant et al. 1988; Burk et al. 1999; Dorman and Koračin 2008; Rahn et al. 2013; Parish et al. 2014). The shallow water Froude number F_r is a dimensionless ratio of the layer wind speed U to the speed of the fastest possible gravity wave $\sqrt{g'H}$, where H is the depth of the layer:

$$F_r = \frac{U}{\sqrt{g'H}}, \quad \text{where} \tag{1.1}$$

$$g' = g\frac{\theta_t - \theta}{\theta}. \tag{1.2}$$

The reduced gravity term g' is defined by using the acceleration of gravity g, the layer potential temperature θ, and the potential temperature at the top of the inversion θ_t (Eq. 1.2). F_r is an important diagnostic for MBL flow that determines if gravity waves can propagate upstream or not. For small values of F_r, the flow is subcritical and gravity waves can propagate in any direction. If $F_r > 1$, the flow is supercritical and discontinuities can exist. In the atmosphere, it has been shown that when $0.5 < F_r < 1$ the flow is transcritical since around a cape or point the flow can transition from subcritical upstream to supercritical downstream (Skyllingstad et al. 2001). F_r is ultimately dependent on the synoptic conditions (Dorman and Koračin 2008).

When the flow is transcritical or supercritical, distinct features may be present. Upstream of a cape or point, the flow decelerates and converges, the MBL thickens, and the surface pressure increases (compression bulge). Downstream of a cape or point, the flow accelerates and diverges, the MBL thins, and the surface pressure decreases (expansion fan). A hydraulic jump can form if the flow transitions from supercritical $F_r > 1$ to subcritical $F_r < 1$. Numerical simulations by Koračin and Dorman (2001) indicate hydraulic features are pronounced near all major points, capes, and bays along the California coastline.

Several studies of the hydraulic behavior of the MBL have used coastal buoy data, (e.g., Halliwell and Allen 1987; Beardsley et al. 1987; Dorman and Winant 2000), numerical simulations (e.g., Rogerson 1999; Dorman and Koračin 2008; Skyllingstad et al. 2001; Koračin et al. 2004; Burk et al. 1999; Pickett and Paduan 2003), and aircraft measurements (e.g., Rogers et al. 1998; Rahn et al. 2013). The most pronounced bend in the California coastline is at the Point Arguello and Point Conception (PAPC) headlands. Numerical simulations conducted by Dorman and Koračin (2008) show an acceleration of the wind speed in the lee of PAPC resulting in an expansion fan into the SBC. Other modeling work

of the MBL off the coast of California have been conducted by Skyllingstad et al. (2001) and Koračin et al. (2004) that identified the importance of the large-scale horizontal PGF to the LLJ and MBL response. Details of the coastal flow are imperative for understanding the physical mechanisms forcing upwelling through Ekman transport and Ekman pumping. Recent work (e.g., Bravo et al. 2016) now considers the partition of upwelling from transport and pumping that is based on high resolution WRF simulations, which are also often used to force ocean models (e.g., Boé et al. 2011; Renault et al. 2012). The potential implications of WRF bias on ocean models, for example, emphasizes the relevance and the importance of understanding model deficiencies.

Chapter Two

Data Sources

2.1) Aircraft Measurements

PreAMBLE focused on analyzing the atmospheric dynamics within the MBL along the coast of southern California (Fig. 2.1). From 16 May to 16 June 2012, the University of Wyoming King Air research aircraft conducted fifteen flights and collected over 50 hours of data (see Table 2.1 for a description of all PreAMBLE flights). PreAMBLE obtained quality data of the coastal MBL under a variety of conditions (made available at http://flights.uwyo.edu/projects/preamble12/). Details of the instrumentation are found at http://flights.uwyo.edu/uwka. Most flights observed the adjustment of the strong northwest flow near PAPC as it transitioned into the SBC. The aircraft also sampled Catalina eddies and the initiation of a southerly surge. Those cases will not be discussed in detail since the focus here is on model inconsistencies of the LLJ near PAPC where most measurements were taken.

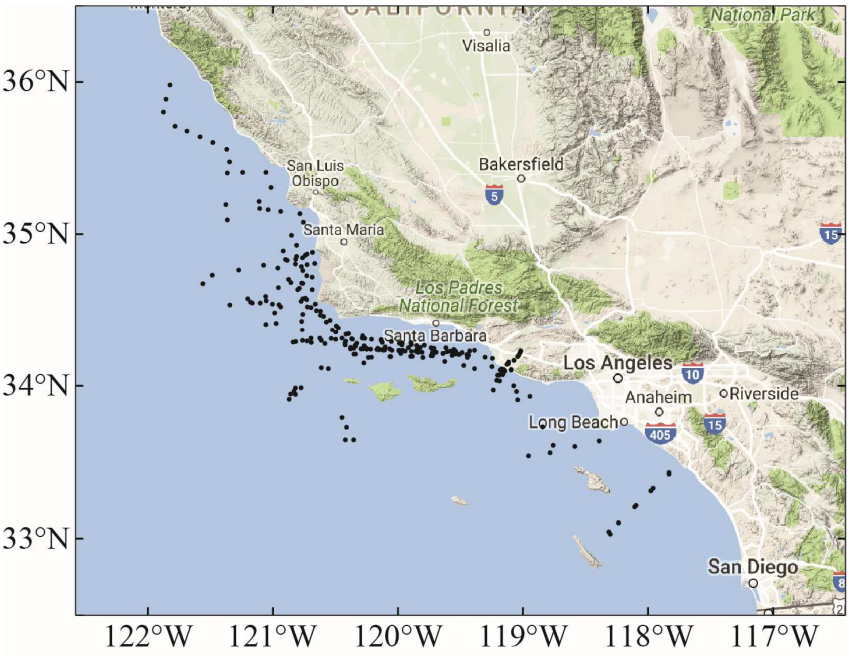

Fig. 2.1: Map of individual PreAMBLE soundings from 16 May to 16 June 2012.

Table 2.1: Summary of PreAMBLE flights including the date and main objective for each event (Rahn et al. 2016). Important locations along the coast are abbreviated as the Santa Barbara Channel (SBC), Point Conception (PC), Point Buchon (PB), and Channel Islands (CIs). Flights with an asterisk (*) have been referred to in recent publications. Flights with a plus sign (+) are the cases analyzed in this paper.

Flight	**Date**	**Objective**
RF01+	16 May	Isobaric pressure field within SBC and north of PC
RF02+	18 May	Isobaric pressure field within SBC and north of PC
RF03*	19 May	Isobaric and vertical profiles around PC
RF04*	20 May	Isobaric pressure field near PC
RF05	24 May (*a*)	Low-level structure upwind of PC and near PB
RF06*	24 May (*b*)	Adjustment of wind and pressure west of SBC
RF07	25 May	Adjustment of wind and pressure west of SBC
RF08	31 May	MBL height and isobaric pressure field of Catalina Eddy
RF09	3 June (*a*)	Isobaric and vertical profiles around PC
RF10*	3 June (*b*)	Adjustment of wind and pressure west of SBC
RF11	6 June	MBL height and isobaric pressure field of Catalina Eddy
RF12*	9 June (*a*)	MBL height and isobaric pressure field of Catalina Eddy
RF13*	9 June (*b*)	Topographic influence of CIs on wind and pressure
RF14*	13 June	Eddy circulation in SBC, low-level structure north of PC to PB
RF15*	16 June	Initiation of southerly surge north of PC

Two primary flight strategies were used. The aircraft flew a series of ascents and descents in a sawtooth pattern to create a cross section of the lower atmosphere. The aircraft also flew at a constant pressure level so that the horizontal PGF could be determined by the slope of the isobaric surface. The first two research flights of PreAMBLE, RF01 and RF02, spent much of the time flying on an isobaric pressure field within the SBC and north of PAPC. Although all data are examined, the data from these two flights are used as case studies in chapter three to highlight the findings.

Several PreAMBLE research flights have already been investigated by a series of case studies in recent publications (Table 2.1). However, only a few analyses include simulations of WRF as a supplement to observations from specific PreAMBLE research flight events (Parish et al. 2014; Parish et al. 2015; Parish et al. 2016). Even though some case studies have had modest success in simulating the observed conditions near PAPC, the model still has difficulty in representing the fine-scale structures of temperature and wind, especially in the SBC (Rahn et al. 2014).

2.2) WRF Model Description

Simulations were conducted with version 3.6.1 of the Advanced Research WRF (ARW, Skamarock et al. 2008) modeling system that is designed for research and operational use. The dynamical core of WRF is suitable for simulations over a broad range of scales from tens of meters to thousands of kilometers. The model is configured with 84 sigma coordinate vertical levels and has a two-way nested grid. The horizontal grid spacing for the parent domain (D1) and inner domain (D2) are 9 km and 3 km, respectively (Fig. 2.2). D2 consists of 195 x 198 grid points and D1 has 201 x 192 grid points. Simulations are initialized with the 12-km North American Mesoscale Model (NAM) analysis grids, which also provide the lateral boundary conditions for the outer domain. A series of 48-hour simulations initialized every 12 hours are conducted from 0000 UTC 1 May 2012 to 2300 UTC 30 June 2012. Model output was generated hourly and the 12 to 23-hour forecast from each 48-hour simulation is used to create a continuous time series for the two-month period. The 24 to 35-hour forecast was also examined, and conclusions are similar to the 12 to 23-hour forecasts.

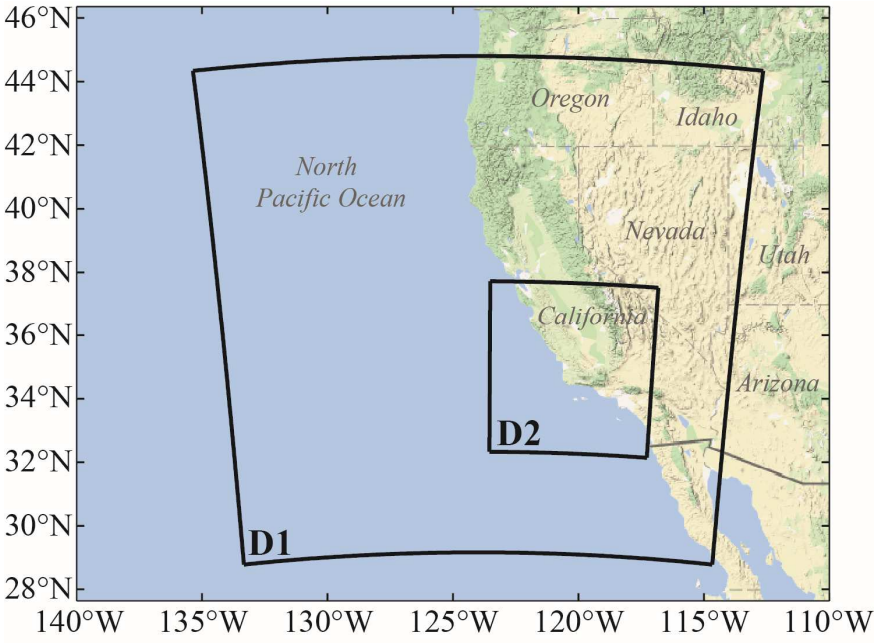

Fig. 2.2: Model domains used in the WRF simulations. The outer domain (D1) and the inner domain (D2) are outlined and correspond to a horizontal resolution of 9 km and 3 km, respectively.

Many physics options are available including microphysics, planetary boundary layer (PBL) schemes, cumulus parameterizations, land-surface model, and radiation. The list of physics and dynamics options used for these simulations are in Table 2.2. The land-surface and PBL schemes are particularly important for this application. Several options for PBL schemes are available and are responsible for representing the fluxes of heat, moisture, and momentum in the boundary layer and the vertical diffusion within the whole column (Skamarock et al. 2008). The appendix includes the namelists that were used to run the WRF Preprocessing System (WPS) and WRF (Table A1 and Table A2, respectively). Simulations of the lower atmosphere offshore of California can be sensitive to the choice of parameterization (Rahn et al. 2014), so a close examination of a PBL scheme is important. To illustrate the PBL sensitivity, a suite of simulations was conducted using 10 different PBL schemes. The simulations only differ by the PBL option and all other settings remain the same, except when the PBL scheme required a specific surface layer model. The vertical profiles of temperature and wind observations from PreAMBLE were compared to simulations from these different PBL parameterizations. An example is shown

in Fig. 2.3 that demonstrates the sensitivity. Each parameterization has different biases, but the shape of the profiles is similar. No choice of PBL was clearly superior. For this study, the Mellor-Yamada-Janjic PBL scheme (highlighted in blue) is used for all WRF simulations run in the analysis during May and June 2012.

Table 2.2: Model physics options and WRF schemes used in the simulations.

Model Physics Options	**WRF Scheme**	**Reference**
Microphysics	Morrison Double-Moment	Morrison et al. (2009)
Longwave Radiation	RRTMG	Iacono et al. (2008)
Shortwave Radiation	RRTMG	Iacono et al. (2008)
Surface Layer	Eta Similarity	Janjic (1994)
Land Surface	Noah Land Surface Model	Tewari et al. (2004)
Planetary Boundary Layer	Mellor-Yamada-Janjic	Janjic (1994)
Cumulus Parameterization	Betts-Miller-Janjic	Janjic (1994)

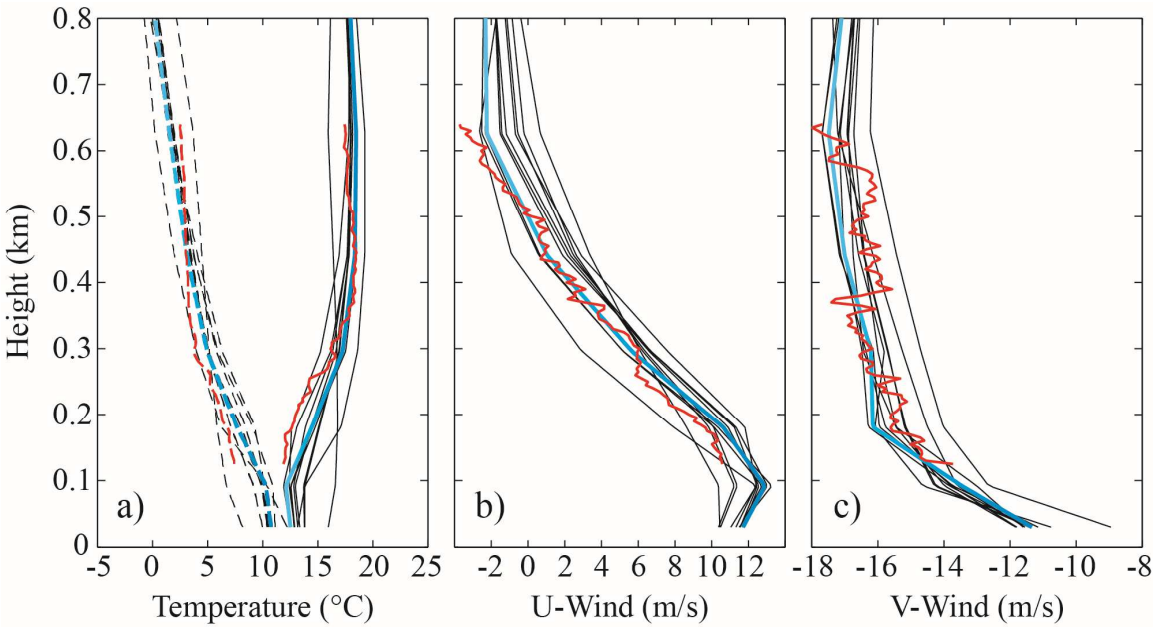

Fig. 2.3: Profiles of the observed (a) temperature (°C, solid red) and dew point temperature (°C, dashed red) and the (b) u- and (c) v-wind (m s^{-1}, solid red) from RF05 at 1445 UTC 24 May 2012 (34.396°N, 120.4919°W, just southwest of Point Conception). Observed soundings are compared to 10 different WRF PBL schemes (black lines) from the 15-hour forecast valid 1500 UTC 24 May 2012. Model output from the Mellor-Yamada-Janjic Scheme is highlighted in blue.

Chapter Three
Evaluation of the WRF Model

3.1) Introduction

Model assessment begins with a comparison to buoy data. A synoptic forcing classification system is developed to test whether the strength of the low-level wind speed influences model performance at several locations along the coast. The simulated low-level structure is assessed using data from PreAMBLE aircraft measurements. The coastal region of southern California is divided into four sub-regions to characterize the wind and temperature profiles. Several mean composite vertical soundings are constructed from WRF output and PreAMBLE aircraft data for each sub-region. The mean composite soundings for each sub-region demonstrates that model performance varies along the coast and indicates the regions where the model is more consistent with observations. The 12-km North American Mesoscale (NAM) model is compared to surface measurements over several years to demonstrate that an operational model shows similar results and tendencies as this higher-resolution WRF configuration. Two research flights from PreAMBLE (16 and 18 May 2012) highlight and support the conclusions from the composites. The case studies focus on the observed and simulated vertical structure of the MBL near PAPC and the near-shore isobaric fields within the SBC. The case studies also highlight the implications for applications such as wave ducting of electromagnetic radiation (Burk and Thompson 1997; Haack and Burk 2001; Haack et al. 2010; Thompson and Haack 2011; Wang et al. 2012).

3.2) Surface Analyses

a. Data Preprocessing

Observations from buoys and coastal stations are recorded hourly. Missing data on the order of 1-3 hours every few days were common. To fill the short gaps ($\leq$ 3 hours), the missing data are replaced by linear interpolation of the surrounding observations to create a continuous data set. Buoy observations are adjusted to a standardized height to uniformly compare the data from all buoys to the 10-m output from the model. Most buoy stations

have an anemometer height of 5 m above mean sea level, except for NDBC buoy 46053 (b-53) and the coastal stations of Port San Luis, CA (b-ps), Point Arguello, CA (b-pt), and Santa Barbara, CA (b-nt). Additional information of each station is in Table 3.1 and the locations are shown in Fig. 3.1. The wind speeds are standardized by using the Power Law Method:

$$u_2 = u_1 \, (z_2/z_1)^P, \tag{3.1}$$

where z_1 is the measurement height, u_1 is the wind speed at measurement height, z_2 is the desired height, and u_2 is the estimated wind speed at the desired height. P is a function of atmospheric stability and surface characteristics, and it is approximately 0.11 for near-neutral conditions over open water (Hsu et al. 1994). The buoy wind speeds are adjusted with this relationship to a standard height of 10 m, which is the output height of the wind speed simulated in WRF. Since the observations do not fall exactly on a grid point, the model output is bilinearly interpolated to the buoy location.

Table 3.1: A list of stations and specifics about the site type (buoy/coastal station), the site elevation (m) above mean sea level, the anemometer height (m) above site elevation, and the latitude (°N) and longitude (°W) of each site. Stations are owned and maintained by NOAA's National Ocean Service (NOS) or the National Data Buoy Center (NDBC).

Operated by	Station ID	Site type/ Elevation (m)	Anemometer Height (m)	Lat (°N)	Lon (°W)
NDBC	46028 (b-28)	buoy/sea level	5	35.71	121.86
NDBC	46042 (b-42)	buoy/sea level	5	36.79	122.45
NDBC	46053 (b-53)	buoy/sea level	4	34.25	119.85
NDBC	46054 (b-54)	buoy/sea level	5	34.27	120.48
NDBC	46069 (b-69)	buoy/sea level	5	33.67	120.21
NOS	NTBC1 (b-nt)	coastal/2.6	13.2	34.41	119.69
NOS	PSLC1 (b-ps)	coastal/sea level	13.6	35.17	120.75
NDBC	PTGC1 (b-pt)	coastal/32.3	9.4	34.58	120.65

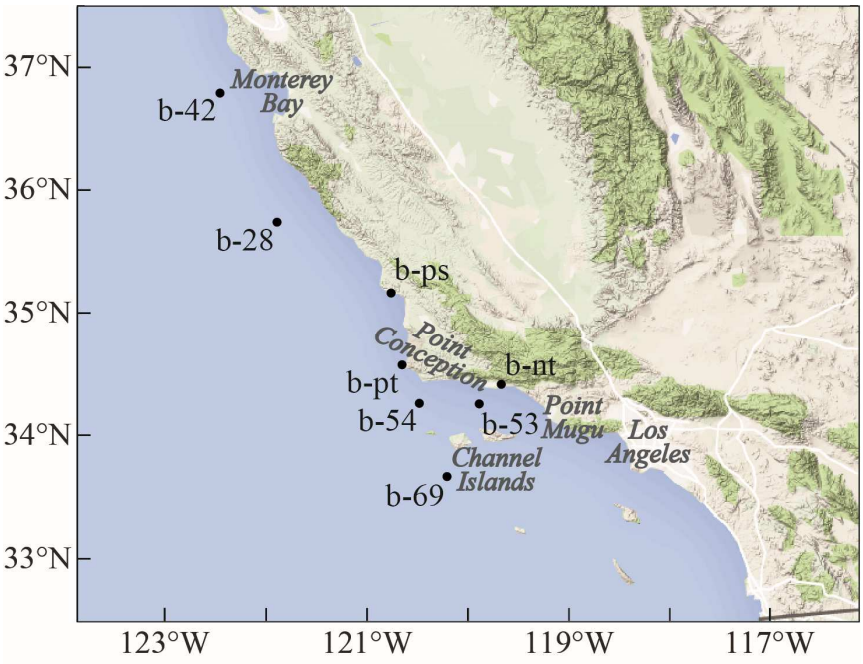

Fig. 3.1: Locations of the buoys and coastal stations mentioned throughout the text. Key regions are identified for geographic reference.

b. Buoy Observations

Two primary geographical regions describe buoy locations. *Upstream* refers to the region north of PAPC and *downstream* refers to the area south of PAPC including the SBC. The distribution of wind speed and direction at three buoy locations along the coast are depicted by wind rose diagrams (Fig. 3.2). Winds are predominantly out of the northwest (304°-326°) during May and June 2012, upstream at b-28 and near PAPC at b-54. Northwesterly winds are reported more than 75% of the time at both buoy stations. Downstream into the SBC, the wind directions are more variable. Winds out of the west are most common at b-53, occurring 33% of the time. Wind speeds are generally much weaker at b-53 than at other locations. Winds from the west at speeds less than 6 m s^{-1} are observed 44% of the time at b-53. The strongest winds occur at b-54 where the flow typically accelerates in the expansion fan and 50% of the northwesterly winds are greater than 12 m s^{-1}. Upstream at b-28 the winds are from the northwest with speeds greater than 10 m s^{-1} more than 60% of the time.

Wind rose diagrams from WRF at the same locations are shown in Fig. 3.2. The greatest difference between the model and observations occurs at b-53, downstream in the SBC, where the model largely overestimates the wind speed. Winds greater than 10 m s^{-1} at b-53 occur 25% of the time in the simulations, but occur only 11% of the time in the observations during the two-month period. Winds in the model are also more frequently out of the west at b-53, but only 22% of these winds are less than 6 m s^{-1}. This is much less than the westerlies in the observations previously noted.

The wind direction varies the most in the SBC between the model and observations. For instance, winds with a southerly component are more common in the observations than the model. Specifically, winds out of the west-southwest and southwest direction (214°-259°) occur 30% of the time in the observations, while only 16% of the time the winds are from this direction in the model. Winds with a northerly component occur more frequently in the model and tend to be stronger than the observations.

Conversely, at b-54 and b-28 the observed winds tend to be stronger than the model winds. The model differs the most at b-54 during strong northwest wind. Winds from the northwest greater than 12 m s^{-1} occur 10% more of the time in the observations than in the model for the entire period. In general, the model overestimates the wind speed downstream of PAPC into the SBC and underestimates the wind speed in locations upstream and near PAPC.

A time-series from 1 May to 30 June 2012 of the along-shore and cross-shore wind at b-28 is shown in Fig. 3.3. Shore-relative wind components were obtained by rotating the u- and v-components -33°. Overestimation of the modeled along-shore wind speed at b-28 is particularly evident during several events over the two-month period. The largest differences occur when the observed along-shore wind speed relaxes, especially in early to mid-May and mid-June. The model greatly overestimates the northerly wind speed when the wind weakens. When strong along-shore wind is observed, differences between the model and observations are reduced. The cross-shore component is generally much weaker in the upstream region since the wind is most frequently out of the northwest during this period.

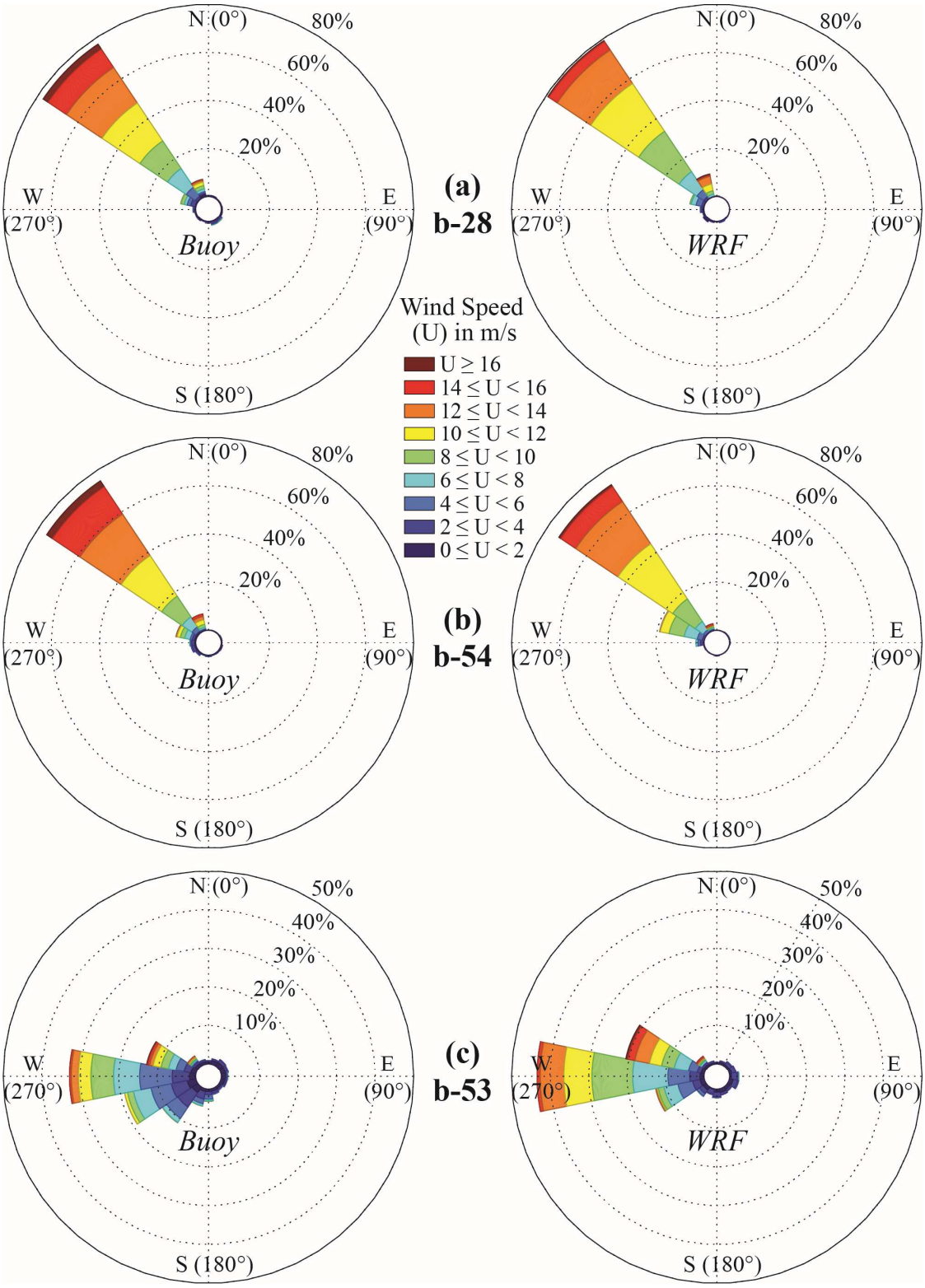

Fig. 3.2: Wind rose diagrams (m s^{-1}) during May and June 2012 at (a) b-28 (top), (b) b-54 (middle), and (c) b-53 (bottom) comparing buoy data (left) to model output (right).

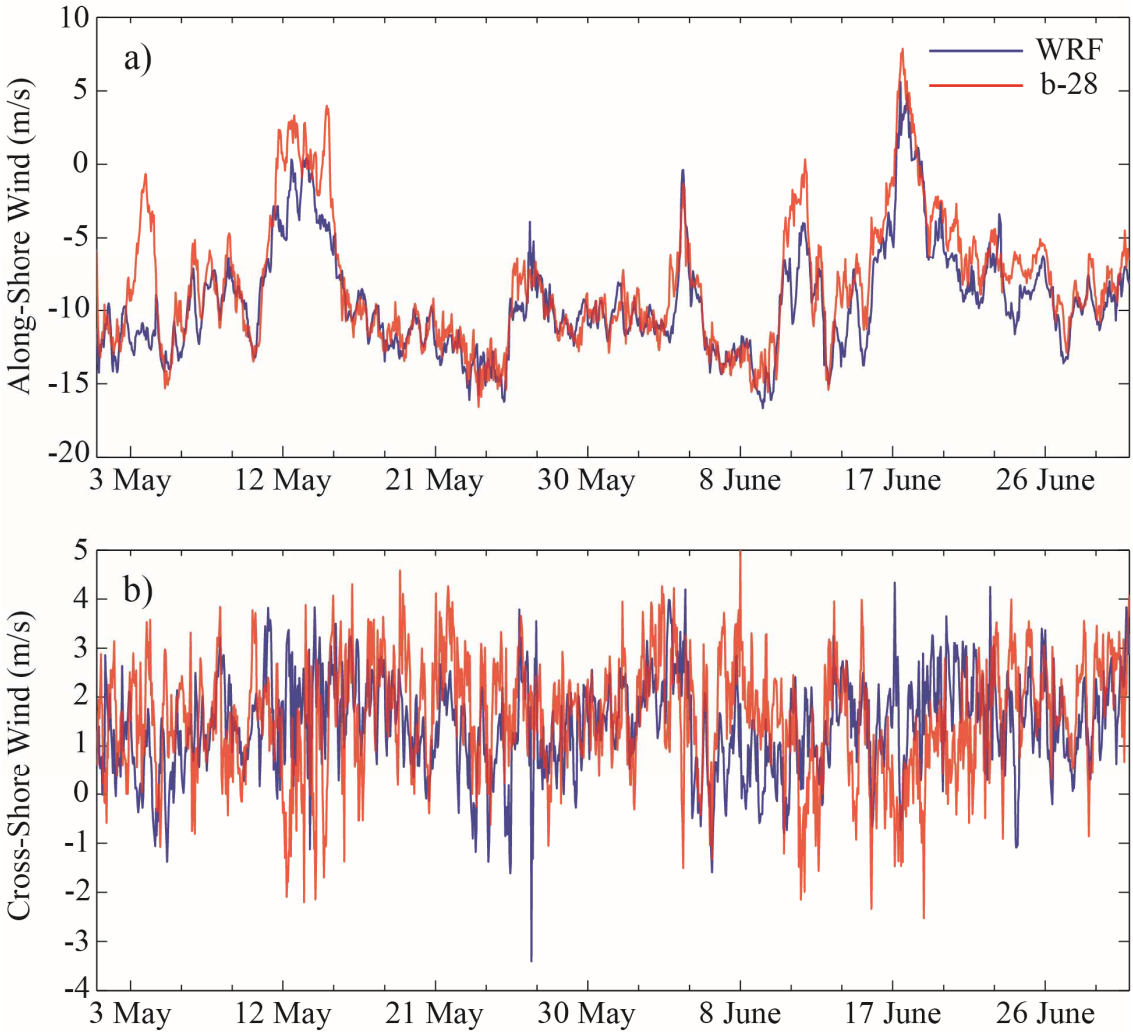

Fig. 3.3: Time series of the (a) along- and (b) cross-shore wind (m s^{-1}) at b-28 from 1 May to 30 June 2012 comparing the observed winds (red) to WRF (blue).

Scatter plots of the wind components show the linearity between the observations and model output (Fig. 3.4). The scatter plots at b-28 indicate that the model has more difficultly with the cross-shore component than the along-shore component. This is in part due to the smaller range of the cross-shore component. The Pearson correlation coefficient *r* is used to measure the linear relationship between WRF and buoy observations, and is defined as the covariance of the two data sets divided by the product of their standard deviations:

$$r = \frac{\sum_{i=1}^{n}(x_i - \bar{x})\,(y_i - \bar{y})}{\sqrt{\sum_{i=1}^{n}(x_i - \bar{x})^2}\sqrt{\sum_{i=1}^{n}(y_i - \bar{y})^2}} \tag{3.2}$$

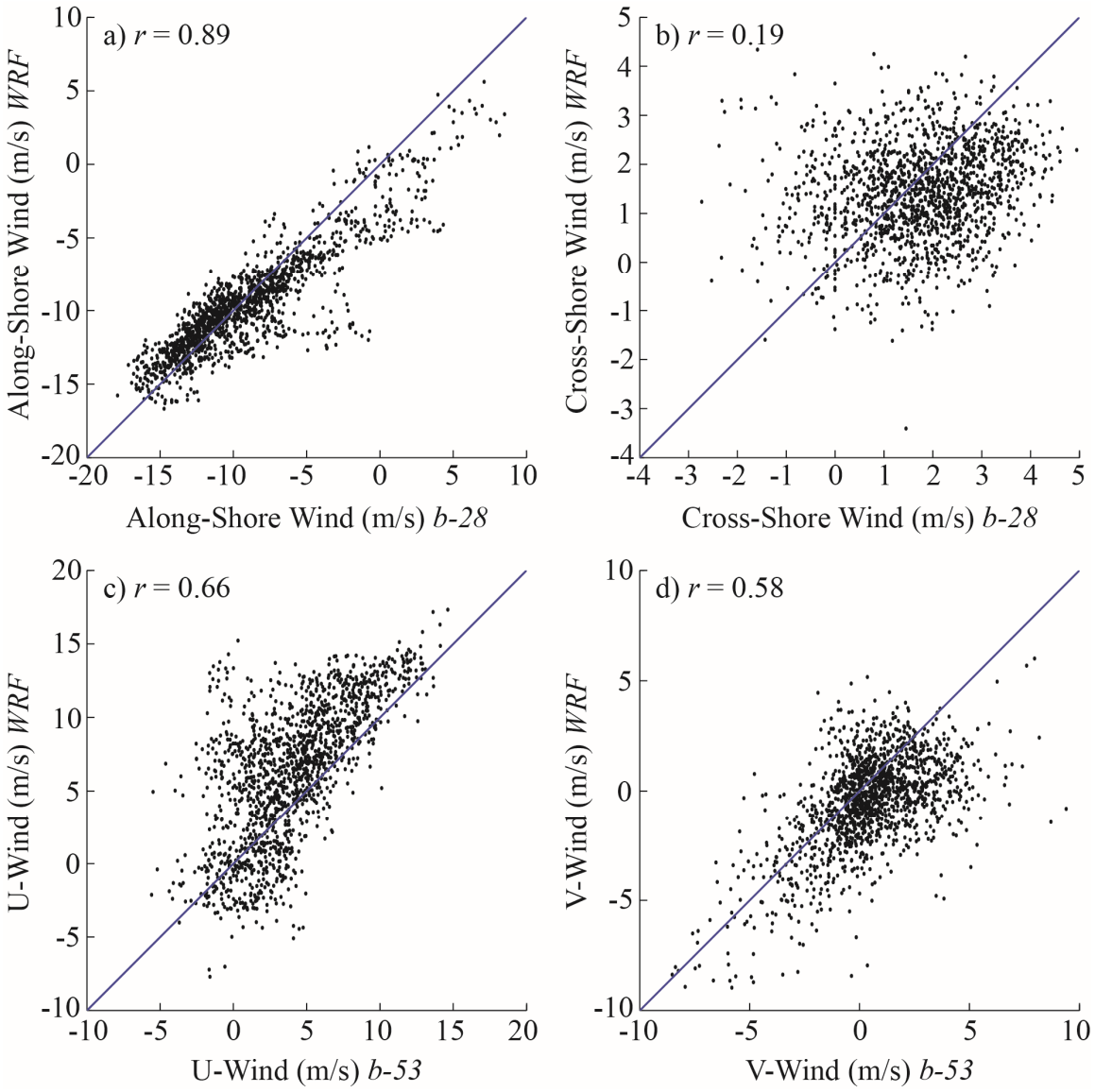

Fig. 3.4: Scatter plots of the (a) along- and (b) cross-shore wind (m s^{-1}) at b-28 and the (c) u- and (d) v-wind (m s^{-1}) at b-53 from 1 May to 30 June 2012 comparing observations to model output. The correlation coefficient is denoted as (r) and the one-to-one reference line is shown in blue.

Over this time, the wind in the along-shore direction from the model is much better than the cross-shore direction with $r = 0.89$ and $r = 0.19$, respectively. In the SBC at b-53, the u and v components of the wind are both poorly simulated. Due to the orientation of the coastline and the location of b-53, the u-component represents the along-shore flow and the v-component resembles the cross-shore flow. Both components of the wind have poor correlation coefficients with $r = 0.66$ and $r = 0.58$ in the u and v, respectively.

Hodographs constructed from mean hourly observations at several buoys and coastal stations reveal the average diurnal cycle. The highest wind speed occurs in the late afternoon at all locations (Fig. 3.5). The smallest diurnal variability is north of PAPC at b-28 and b-42. In the lee of PAPC at b-54, the wind exhibits a nearly circular diurnal cycle, similar to Dorman and Winant (2000). Further to the southeast, b-69 also exhibits a circular diurnal pattern, though slightly weaker. Diurnal variability is notably different in the SBC. The hodograph at b-53 is almost completely zonal with a weak southerly component on average. Similar features exist at coastal station b-ps, where the wind is mostly zonal despite a weak northerly mean flow. In contrast, the low-level flow near coastal station b-pt is relatively strong and nearly entirely meridional with a weak easterly component.

The diurnal cycle of the wind is compared to the numerical simulations at four buoy stations along the coast (Fig. 3.6). The mean wind is removed to isolate the differences in the diurnal cycle. The upstream buoys (b-42 and b-28), display a similar elliptic hodograph structure with the major axis aligned along the coast, and the strongest northwest winds during the afternoon hours. The model output is similar to the observations for these buoys located upstream. Near Point Conception at b-54, the hodograph is more circular with the largest hourly anomalies in the region. At b-54, the model largely underestimates the magnitude of the hourly wind anomaly for most hours of the day, and differences are especially prevalent when the strongest wind speeds are observed from 1800 UTC [1100 Pacific Daylight Time (PDT)] to 0600 UTC (2300 PDT). Underestimation of wind speed in WRF depicted by the hodograph at b-54 is consistent with the wind rose (Fig. 3.2).

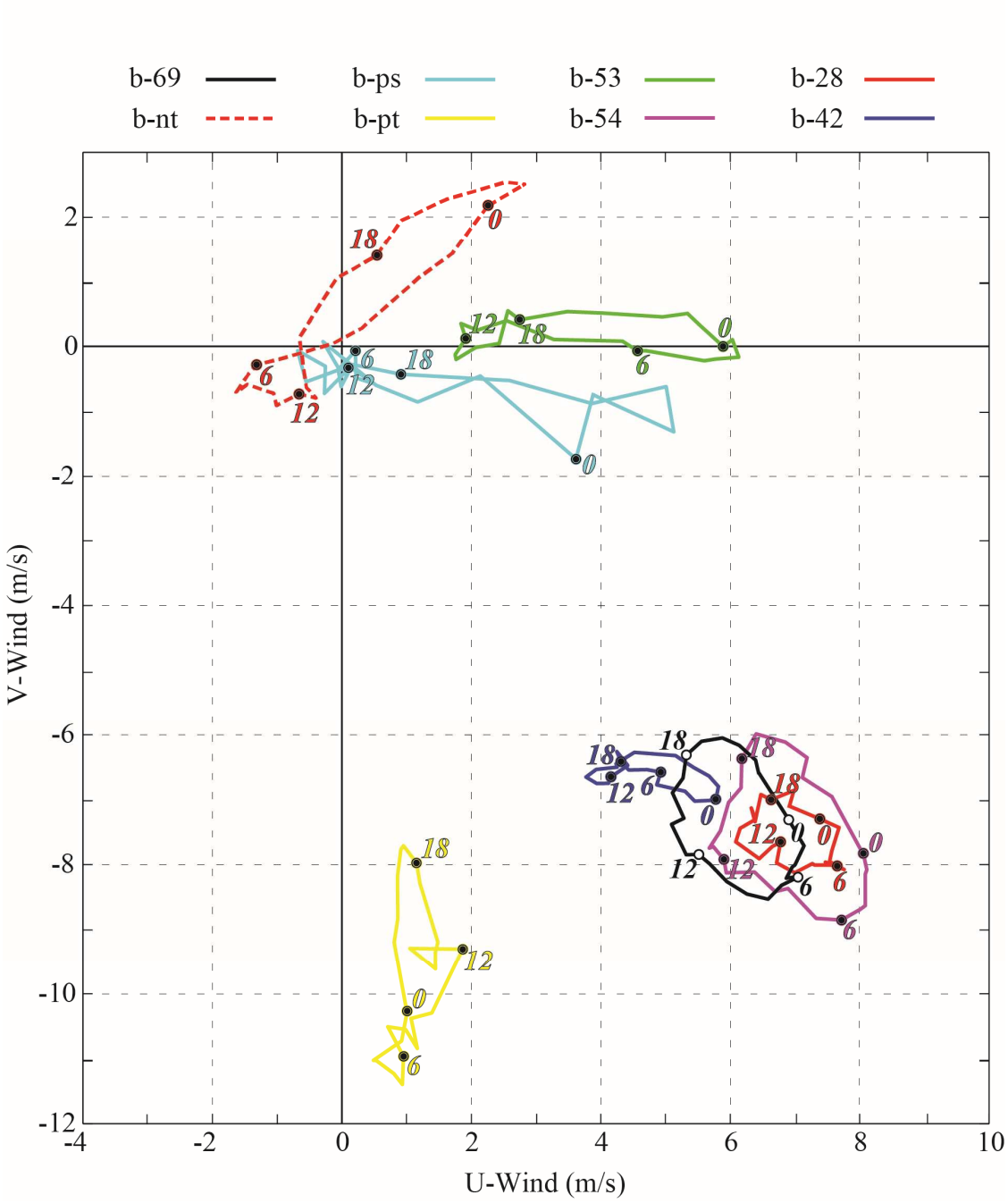

Fig. 3.5: Hodographs of the mean diurnal wind speed (m s^{-1}) during PreAMBLE at several buoys and coastal stations. Time of day (UTC) is labeled every 6 hours.

At b-53 in the SBC, the mean wind direction is primarily in the u-direction (Fig. 3.5) and the average diurnal variation occurs almost all in the zonal wind component. The v-wind represents onshore and offshore (cross-channel) flow at b-53. Despite little diurnal

variation of the observed mean meridional wind, the model has greater variability, especially during the late morning to early afternoon from 1800 UTC (1100 PDT) to 2100 UTC (1400 PDT) and at night from 0600 UTC (2300 PDT) to 0900 UTC (0200 PDT). The discrepancy between the model and observations at b-53 located in the SBC is explained in more detail after presenting the aircraft observations.

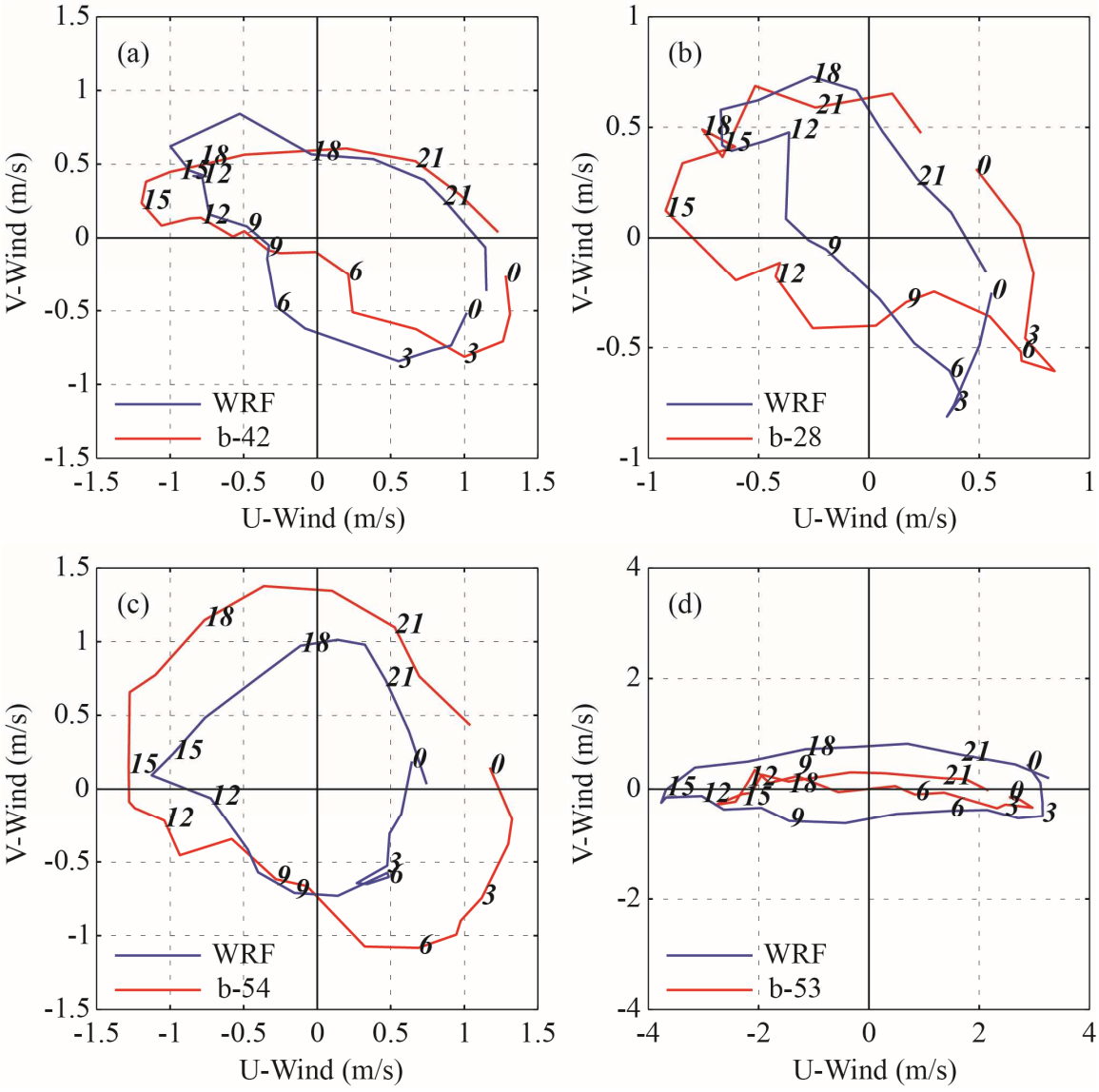

Fig. 3.6: The observed (red) and modeled (blue) diurnal (mean removed) hodographs (m s^{-1}) at (a) b-42, (b) b-28, (c) b-54, and (d) b-53 during May and June 2012. Time of day (UTC) is labeled every 3 hours.

Box-and-whisker diagrams of the u- and v-wind components at b-28 and b-53 are shown in Fig. 3.7 and depict the mean, median, interquartile range, and upper and lower 10% of the data. The upstream region represented by b-28 in Fig. 3.7a displays relatively good agreement in terms of the mean u- and v-wind components between the model and observations. The mean u-wind at b-28 is 6.3 m s^{-1} and 6.3 m s^{-1} for the buoy observations and the model, respectively. Likewise, the mean observed v-wind at b-28 is -6.6 m s^{-1} and the mean modeled v-wind is -7.2 m s^{-1}. The modeled and observed data sets for the u- and v-wind at b-28 have a high correlation coefficient of greater than 0.8 and a root mean square error (*RMSE*) near 1.9 m s^{-1}. The *RMSE* is the difference between the observed value X_{obs} and the predictor value X_{model}, as shown in Eq. 3.3. Additional metrics including the median, standard deviation, correlation coefficient, and *RMSE* are provided in Table 3.2 for b-42, b-28, b-54, and b-53.

$$RMSE = \sqrt{\frac{\sum_{i=1}^{n} (X_{obs(i)} - X_{model(i)})^2}{n}} \tag{3.3}$$

The meridional and zonal winds in the downstream region, characterized by b-53 in Fig. 3.7b, indicate less agreement between the observations and the model, especially for the u-wind component. WRF overestimates the magnitude of the along-shore flow in the SBC. The mean u-wind observed by b-53 and the mean u-wind from WRF is 4.4 m s^{-1} and 6.2 m s^{-1}, respectively. The median u-wind of the model is nearly the same magnitude as the upper quartile of the buoy observations, resulting in a poor correlation coefficient and a *RMSE* of 3.65 m s^{-1} at b-53. The model also struggles with the v-wind at b-53, which is the cross-shore component in this location. Although the v-wind is weak on average, the mean simulated v-wind is northerly and the observed v-wind is southerly. Thus, the v-wind correlation coefficient is poor and the *RMSE* is 2.1 m s^{-1}.

Table 3.2: Statistical comparison between buoy observations and WRF simulations for the u- and v-wind (m s^{-1}): STD = standard deviation, COR = correlation coefficient, RMSE = root-mean-square-error.

	Buoy U-Wind			WRF U-Wind				
Station	**Mean**	**Median**	**SD**	**Mean**	**Median**	**SD**	**COR**	**RMSE**
b-42	4.37	4.81	2.50	4.73	4.99	1.96	0.72	1.73
b-28	6.31	6.94	3.15	6.34	6.68	1.98	0.82	1.91
b-54	7.08	7.54	2.85	7.71	8.21	2.14	0.77	1.83
b-53	4.40	4.11	3.92	6.24	6.85	4.70	0.67	3.65
	Buoy V-Wind			**WRF V-Wind**				
Station	**Mean**	**Median**	**SD**	**Mean**	**Median**	**SD**	**COR**	**RMSE**
b-42	-5.71	-6.79	3.89	-5.75	-6.18	3.20	0.82	2.21
b-28	-6.58	-7.33	3.37	-7.16	-7.60	3.21	0.86	1.88
b-54	-7.25	-8.05	3.74	-6.72	-7.04	2.83	0.86	1.94
b-53	0.46	0.43	2.30	-0.50	-0.24	2.18	0.58	2.06

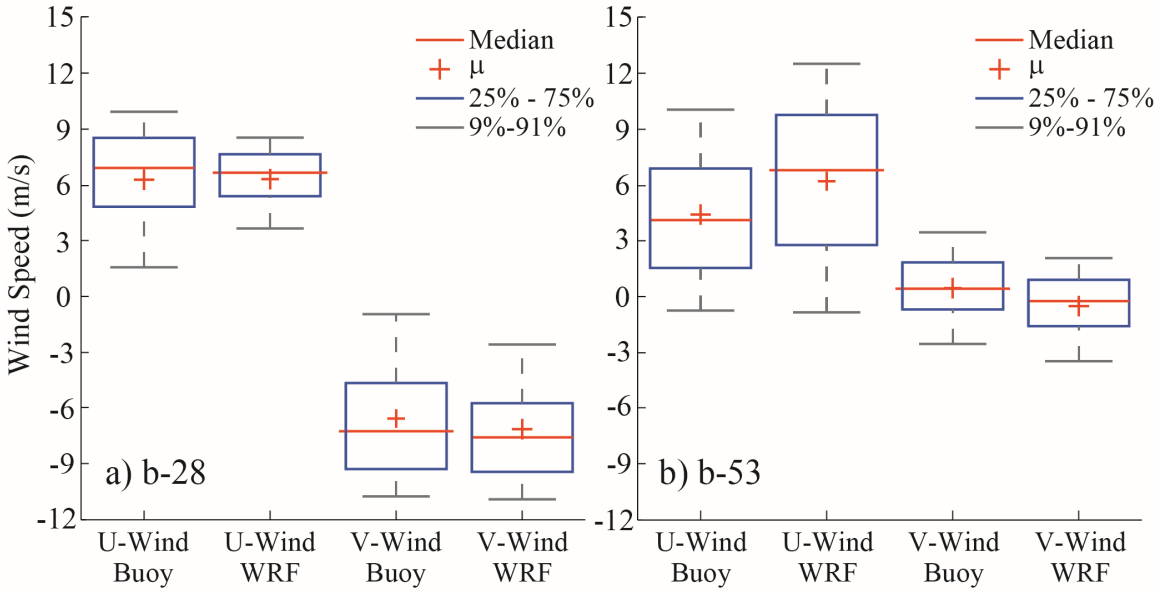

Fig. 3.7: Box-and-whisker diagrams of the u- and v-wind (m s^{-1}) at (a) b-28 and (b) b-53 during May and June 2012 comparing observations to model output. The mean (μ) of the data sets are denoted by (+) in each diagram.

To better understand the distribution of winds, kernel density smoothing is applied to the buoy and WRF winds. This technique is a nonparametric approach to estimate the probability density function of a data set. The kernel density estimate (KDE) is similar to the histogram but illustrates the frequency distribution with a smooth and continuous curve instead of using discrete rectangular bins. The KDE uses Gaussian-shaped kernel estimates at each sample point, and the resulting distribution curve is obtained by adding the densities of these individual kernels. KDE curves are constructed for the u- and v-wind at b-28 and b-53, and estimates the probability density at x as:

$$f(x) = \frac{1}{n}\sum_{i=1}^{n} K_h(x - x_i)\,, \tag{3.4}$$

where K_h(x) is the Gaussian kernel function with smoothing parameter (bandwidth) h, given by:

$$K_h(x - x_i) = \frac{1}{\sqrt{2\pi}\,h} \mathrm{e}^{-\frac{1}{2}\left(\frac{x - x_i}{h}\right)^2}. \tag{3.5}$$

The degree of smoothing applied to the KDE curve depends on the size of the selected bandwidth. If h is too large, the resulting density curve will be over-smoothed from greater averaging and will be less sensitive to small-scale variation. As h decreases, the density estimates become more sensitive to small variations of the data sample and will produce a wavy KDE curve with higher variability. The density curves shown Fig. 3.8 represent the density distribution for the u- and v-wind at b-58, b-54, and b53. These KDE curves are constructed using small bandwidths with a smoothing parameter value of less than one for all density curves ($0 < h < 1$).

The frequency distribution for the simulated and observed u-wind at b-28 (Fig. 3.8a) and b-54 (Fig. 3.8c) have peaks in the same location with most speeds between 5-10 m s^{-1}. The observed wind has a broader distribution and the tails of the distribution extend well beyond the simulated distribution. There is better agreement of the modeled and observed

distribution of v-wind at b-28 (Fig. 3.8b), especially when the wind is strong. As the v-wind weakens (> -10 m s^{-1}), the KDE of the model deviates from observations. The v-wind near PAPC at b-54 (Fig. 3.8d) is largely underestimated by the model. The distribution of this KDE curve has a greater frequency of stronger meridional winds especially around its peak density.

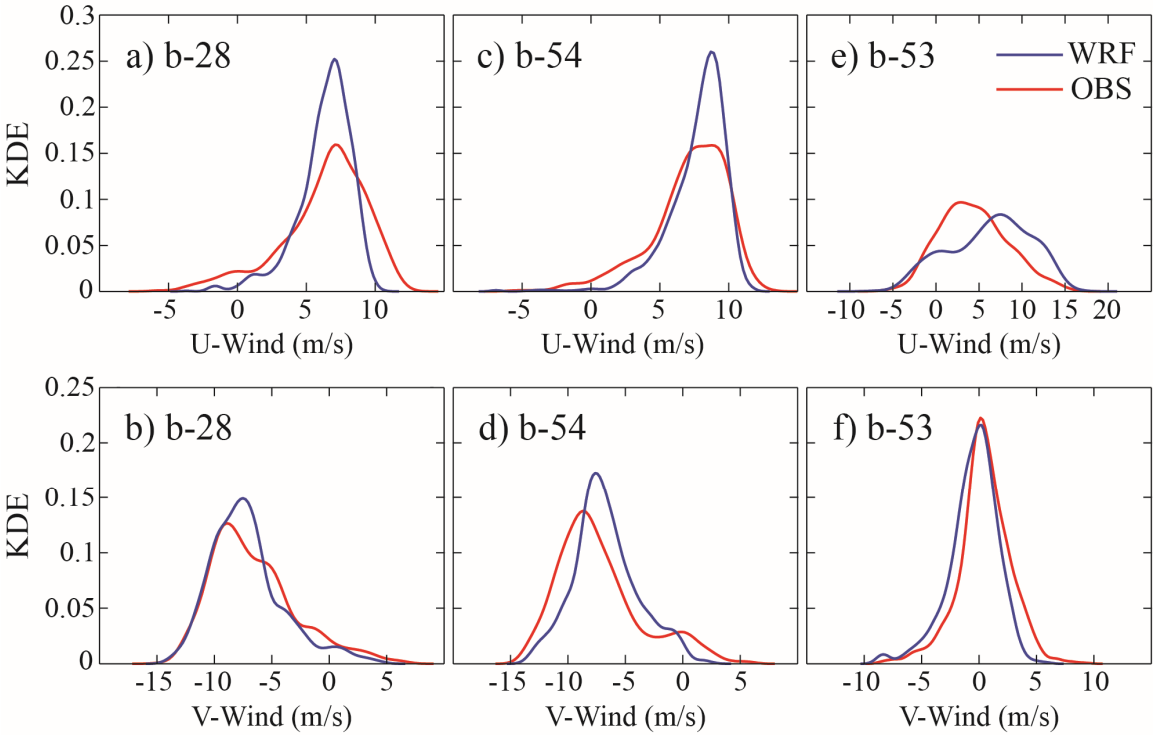

Fig. 3.8: Kernel Density Estimation (KDE) curves of the u- and v-wind (m s^{-1}) during May and June 2012 for observations (red) and WRF (blue): (a) u-wind at b-28, (b) v-wind at b-28, (c) u-wind at b-54, (d) v-wind at b-54, (e) u-wind at b-53, (f) v-wind at b-53.

In the SBC at b-53, the distribution of the simulated u-wind is shifted to the right of the buoy winds, indicating a stronger westerly wind than observed (Fig. 3.8e). Observed u-wind has a peak closer to zero, with a higher frequency of u-winds of 0-5 m s^{-1}. Greater zonal wind in the model at b-53 is consistent with previous plots, which reflects the model's erroneous tendency for the high winds in the expansion fan near PAPC to extend farther into the SBC than observed. The density curves for the v-wind at b-53 represent the distributions of the cross-shore flow in the SBC (Fig. 3.8f). Even though good agreement

may be apparent since both distributions are closely centered on zero, the mean difference between the simulated and observed meridional wind is statistically significant at the 5% significance level performed by Welch's t-test. Observations have a KDE maximum that is positive (mean = 0.46 m s^{-1} and median = 0.43 m s^{-1}), whereas simulations indicate a density peak that is negative (mean = -0.50 m s^{-1} and median = -0. 24 m s^{-1}). Northerly winds are more likely in the model than what occurs at b-53.

c. Influence of Synoptic Forcing

Synoptic atmospheric conditions set up the large-scale PGF that drives the low-level flow along the California coast. When the flow is fast and the MBL depth is shallow (high F_r), hydraulic features such as a compression bulge or an expansion fan can form near coastal points and capes. Since during the warm season F_r is frequently favorable for the development of an expansion fan near PAPC (i.e., not subcritical), there is often a local wind maximum near b-54 (Dorman and Koračin 2008). Therefore, the strength of the large-scale forcing not only drives the speed of the mean wind, but it also impacts the mesoscale response of the coastal wind to changes in the coastline so that there can be locally enhanced wind maxima if the flow is not subcritical.

Surface wind speed and direction offshore of California are inferred from the Advanced Scatterometer (ASCAT) instrument on the EUMETSAT MetOp-A satellite (EUMETSAT 2015). Typical differences between strong, moderate, and weak events along the coast of California are illustrated in Fig. 3.9. The largest spatial changes under the different synoptic forcing are the size and position of the wind maxima around PAPC, which reflects the different mesoscale responses near the coast.

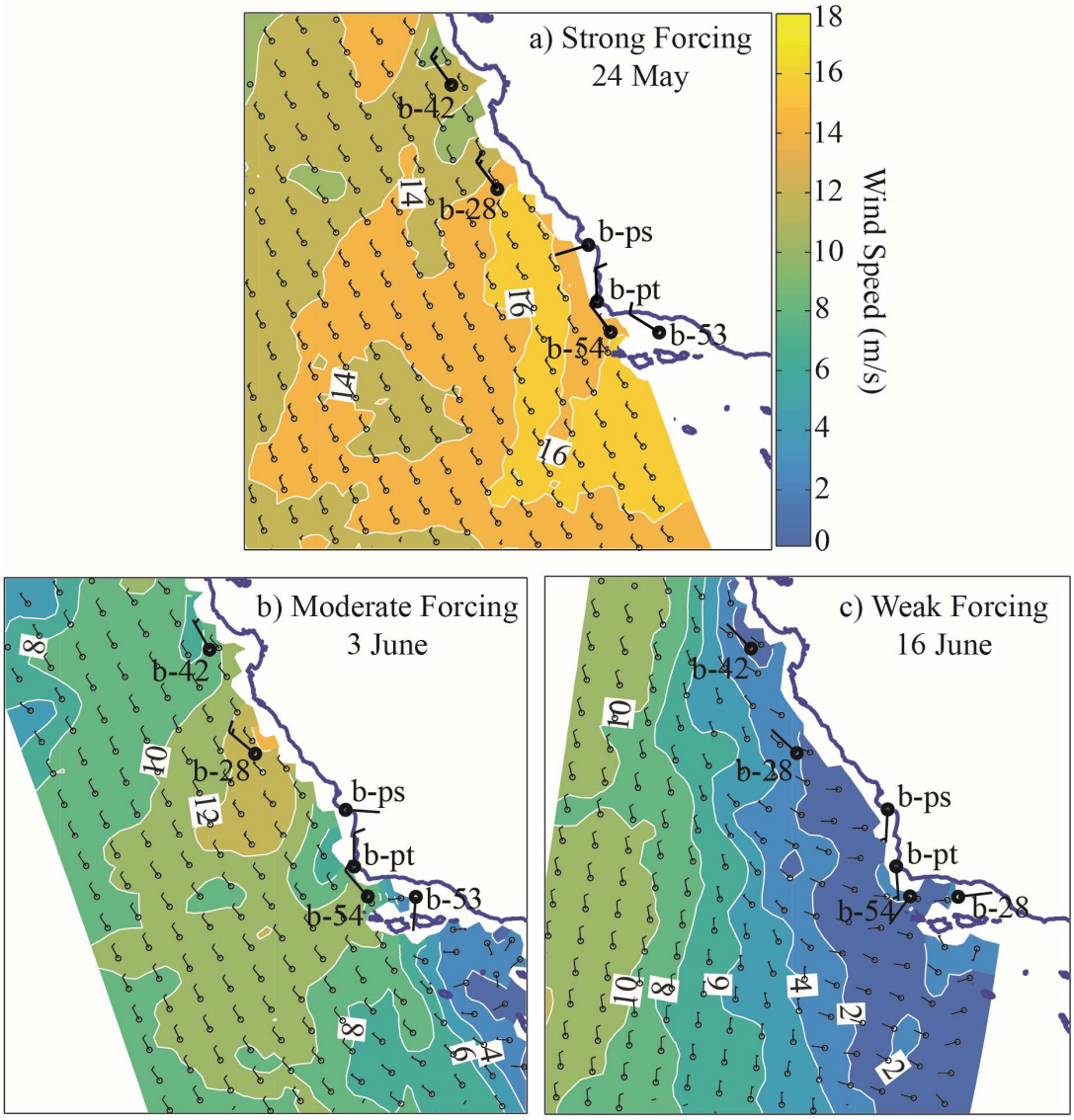

Fig. 3.9: The ocean surface wind speed (m s^{-1}) on (a) 0450 UTC 24 May, (b) 0445 UTC 3 June, and (c) 1735 UTC 16 June 2012 during a strong, moderate, and weak synoptic forcing event, respectively. Data retrieved from the Advanced Scatterometer (ASCAT) Satellite (Center for Satellite Application and Research).

On 24 May 2012 (Fig. 3.9a), strong winds (~14-16 m s^{-1}) extend well offshore with a broad wind speed maximum near the coast of PAPC that extends southward. On 3 June 2012 (Fig. 3.9b), there was moderate forcing with wind speeds slightly less in magnitude (~10-12 m s^{-1}) than during the strong event. The transition between the compression bulge and expansion fan near PAPC is more noticeable in the moderate case. The wind maximum

south of PAPC is more confined to the immediate vicinity. An example of weak synoptic forcing is on 16 June 2012 (Fig. 3.9c). Wind speeds along the coast are considerably reduced (~2-4 m s^{-1}) and the wind speed increases well offshore. These cases depict the differences in not only the magnitude of the wind, but also the spatial distribution of the wind speed maximum. Further comparison with scatterometer data are inhibited by the near-shore contamination of the signal and infrequent satellite passes.

A metric is developed to characterize the strength of the daily synoptic forcing as either strong, moderate, or weak. These cases are assessed independently to determine the impact large-scale atmospheric forcing has on model performance. The definitions here are similar to those defined by Dorman and Koračin (2008). The synoptic forcing for each day is based on the strength of the mean daily wind speed at several buoy stations (Table 3.3). Supplementary material about the methods used for this metric are provided in the Appendix and include the mean wind speed at all buoy stations as well as the designated forcing strength for each day during May and June 2012 (Table A3). The wind magnitudes upstream at b-42 and b-28 are more directly affected by the strength of synoptic forcing because there is less variation in the coastline than near PAPC. Wind speed at b-54 helps the metric definition because the buoy is in the immediate lee of PAPC where the winds usually exhibit the largest diurnal variability (Fig. 3.6c).

During strong synoptic forcing, high wind speeds extend well to the north and south of PAPC. A strong forcing event is defined by the mean daily wind speed $U \geq 11$ m s^{-1} at b-42, b-28, and b-54. Another condition for strong forcing is that the diurnal range of the hourly wind observations at b-54 must be relatively small ($U_{range} < 4$ m s^{-1}), which indicates the flow is fast and persistent for most of the day with minimal variability. A strong forcing event must also have a minimum hourly daily wind speed $U_{min} \geq 7$ m s^{-1}. For moderate wind cases, the wind speed maxima near PAPC are reduced and classified with observed wind speeds between $5 < U < 11$ m s^{-1} at b-42, b-28, and b-54. The diurnal range at b-54 is typically large ($U_{range} \geq 4$ m s^{-1}) during moderate forcing. Minimum wind speeds are common around sunrise before solar heating over land increases the horizontal temperature gradient and accelerates the flow ($U_{min} < 7$ m s^{-1}), and peak wind speeds occur in the late afternoon around 0000 UTC (1800 PDT). A weak wind event has $U < 5$ m s^{-1} at b-42, b-

28, and b-54. This is the only case where the mean diurnal wind speed at b-53 may be greater than any other buoy station. These definitions produce 19 strong, 33 moderate, and 9 weak diurnal events during May and June 2012. It is important to note that only a majority (3 out of 5) of the criteria are needed to define the synoptic forcing strength of each day.

Table 3.3: The diurnal synoptic forcing classification throughout May and June 2012 defined by the strength of the wind at several buoy stations: U = mean diurnal wind speed, U_{max} = wind speed maximum, U_{min} = wind speed minimum, $U_{range} = (U_{max} - U_{min})$ = diurnal range. Refer to Fig. 3.1 for a map of buoy locations.

Diurnal Synoptic Forcing Classification

Strong	Moderate	Weak
▪ $U \geq 11$ m s^{-1} at b-42	▪ $5 < U < 11$ m s^{-1}	▪ $U \leq 5$ m s^{-1} at b-42
▪ $U \geq 11$ m s^{-1} at b-28	▪ $5 < U < 11$ m s^{-1}	▪ $U \leq 5$ m s^{-1} at b-28
▪ $U \geq 11$ m s^{-1} at b-54	▪ $5 < U < 11$ m s^{-1}	▪ $U \leq 5$ m s^{-1} at b-54
▪ $U_{range} < 4$ m s^{-1} at b-54	▪ $U_{range} \geq 4$ m s^{-1} at b-54	▪ U at b-53 > U at any one or more buoys
▪ $U_{min} \geq 7$ m s^{-1} at b-54	▪ $U_{min} < 7$ m s^{-1} at b-54	▪ $U_{max} < 7$ m s^{-1} at b-54
▪ 19 days	▪ 33 days	▪ 9 days

The synoptic forcing metric is applied to the buoy wind observations. Differences between WRF simulations and observations are examined for each forcing regime. This analysis focuses on the buoys surrounding PAPC and includes b-28 and b-42 upstream, b-54 adjacent to PAPC, and b-53 in the SBC. The *RMSE* is calculated at each buoy for every hourly wind speed observation during May and June 2012. To compare the errors between each buoy, the normalized root mean square error (N_{RMSE}) is determined by dividing the *RMSE* by the data set mean of the observations ($\overline{X_{obs}}$) shown in Eq. 3.6.

$$N_{RMSE} = \frac{RMSE}{\overline{X_{obs}}} \tag{3.6}$$

The underlying assumptions to consider when assessing *RMSE* values are that the errors are unbiased and follow a normal distribution. One disadvantage of using the *RSME* is its sensitivity to outliers. Although outliers with several orders of magnitude difference from surrounding data points should be removed, the sensitivity of the *RMSE* to outliers becomes less significant for large data sets comprising more than 100 sample points *n* (Chai and Draxler 2014). The utilization of the *RMSE* to the buoy data sets in this study are sufficiently large enough ($n > 1000$) so that the sensitivity of *RMSE* to outliers is reduced.

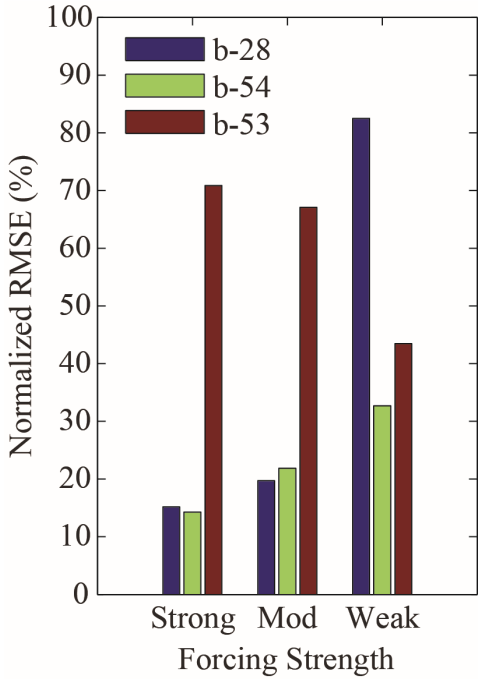

Fig. 3.10: Bar plot showing the N_{RMSE} of the wind speed (m s^{-1}) at b-28 (blue), b-54 (green), and b-53 (red) for strong, moderate, and weak forcing events.

In the SBC at b-53, the normalized error under strong and moderate synoptic forcing between the model and observations is substantially larger than compared to the other buoys' N_{RMSE} (Fig. 3.10). The greatest error at b-53 is during strong synoptic forcing events. The percent of error decreases during moderate to weak forcing events, but the relative normalized error remains high. The best model performance with the least N_{RMSE} is at b-54, where the percent of error during strong and moderate forcing events is near 20% and 33%, respectively. Upstream of PAPC at b-28, model performance is best during strong

and moderate forcing conditions. However, poor model performance occurs during weak synoptic events representing a high N_{RMSE} of 83%.

The N_{RMSE} at b-53 is exceptionally high. The daily average observed wind speed during May and June 2012 at b-53 is about 5 m s^{-1} under all forcing conditions. This is about half the magnitude observed 55 km to the west at b-54 (~10 m s^{-1}). While the data set is large enough to discount outliers as a major influence, the magnitude of wind is small and marginal deviations may be weighted too heavily resulting in a large *RMSE*. The *RMSE* can be separated into the systematic and unsystematic bias. A good model with a low *RMSE* value should have an unsystematic error $RMSE_U$ close to the *RMSE* value and a systematic error $RMSE_S$ should approach zero. The systematic and unsystematic component of the *RMSE* are shown in Eq. 3.7 and 3.8.

$$RMSE_S = \left[\frac{1}{N}\sum_{i=1}^{N}\left|\widehat{\mathrm{X}}_{wrf\,(i)} - \mathrm{X}_{obs\,(i)}\right|^2\right]^{1/2} \tag{3.7}$$

$$RMSE_U = \left[\frac{1}{N}\sum_{i=1}^{N}\left|\mathrm{X}_{wrf\,(i)} - \widehat{\mathrm{X}}_{wrf\,(i)}\right|^2\right]^{1/2} \tag{3.8}$$

To find a linear systematic bias, a linear least-squares regression is performed on each set of hourly data to find the intercept and slope of the linear relationship: $\widehat{\mathrm{X}}_{wrf\,(i)} = a + b\,\mathrm{X}_{obs\,(i)}$. The unsystematic bias can be interpreted as an estimate of how much of the error between the model and observations is due to random noise. The systematic component of the error can come from various error sources such as the parameterizations of subgrid-scale processes, of which greatest discrepancies are usually near the surface (Mass et al. 2008). Some amount of systematic bias is present in the model under each forcing category.

Model bias of the 10-m wind speed during the full two-month period at b-53, b-54, and b-28 is shown in Fig. 3.11a. Large differences between the model and observations of the wind speed occur in the SBC at b-53 with a total *RMSE* of 3.6 m s^{-1}. The total *RMSE* is the sum of the $RMSE_U$ and the $RMSE_S$ components, expressed as:

$$RMSE = \sqrt{RMSE_U^2 + RMSE_S^2}. \quad (3.9)$$

The wind speed *RMSE* components at b-53 are $RMSE_U$ = 3 m s^{-1} and $RMSE_S$ = 1.8 m s^{-1}. The unsystematic bias component is clearly the dominate factor contributing to the relatively high *RMSE* value at b-53. The large unsystematic bias makes up 72% of the total error while the systematic bias counts for only 28%. Since most of the difference between the buoy observations and WRF is not systematic, the errors cannot be easily removed (i.e., apply a linear correction) to improve the forecast. The *RMSE* values at b-54 and b-28 are relatively close to each other with an error near 2.1 m s^{-1}. The amount of error due to random noise is 65% at b-28 and 58% at b-54, and the systematic difference is 35% and 42% at b-28 and b-54, respectively. Since the amount of error is noticeably larger at b-53 than at the other buoys, the *RMSE* is calculated for the u- and v-components of the wind (Fig. 3.11b). Much of the wind speed error occurs in the zonal direction of the flow. The *RMSE* for the u-wind is 4.1 m s^{-1} and the *RMSE* for the v-wind is 2.3 m s^{-1}. The unsystematic component of the error is 76% for the u-wind and 61% for the v-wind component.

The *RMSE* is also evaluated for the wind speed during weak forcing events to address the large increase in the normalized error at b-28 previously shown in Fig. 3.10. It is found that 74% of the error is due to an unsystematic bias, which may be interpreted as random error. The $RMSE_U$ and $RMSE_S$ at the other buoys were nearly the same during weak events when compared to the full time period. Random noise contributes a large portion to the model discrepancies during weak wind periods. WRF underperforms the most when the magnitude of the wind is low. Not only is this true in the SBC (b-53), but the model also shows large deviations from the observations upstream of PAPC during weak events. Simulations come into better agreement with observations when the synoptic forcing is stronger near the region surrounding b-28 and b-54. Since the strength of the synoptic forcing has minimal effect on the wind speed in the SBC (b-53), the wind speed remains weak over the entire period and model performance is poor. This supports the hypothesis

that under weak synoptic forcing events, more complex mesoscale features confound the model solution.

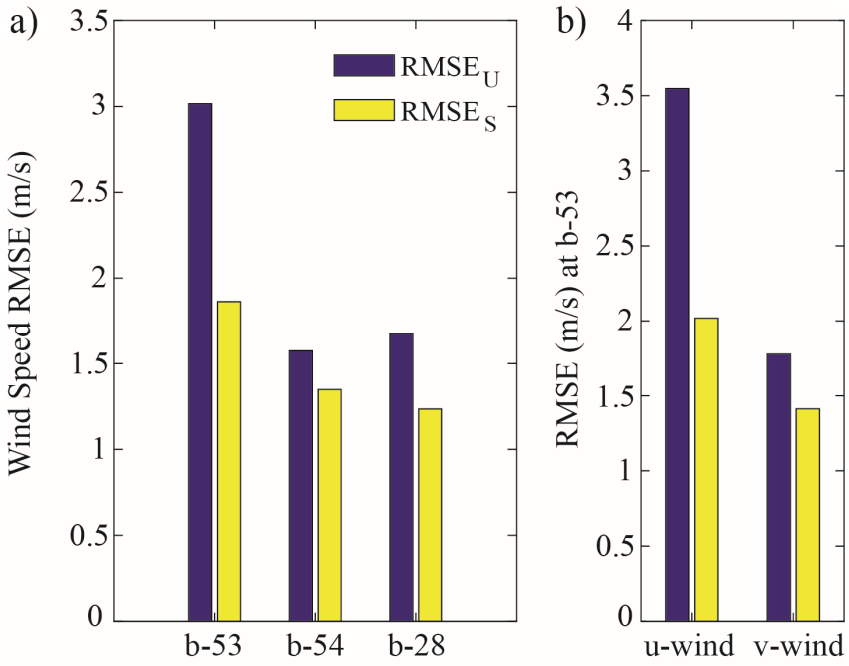

Fig. 3.11: Bar plots of the unsystematic ($RMSE_U$, blue) and systematic ($RMSE_S$, yellow) components of the *RMSE* for the (a) wind speed (m s^{-1}) at b-53, b-54, and b-28 and the (b) u- and v-wind (m s^{-1}) at b-53. The *RMSE* values are calculated using the full data set from May and June 2012.

d. Comparison to the NAM Model

To put these results in context of an operational forecast model, output from the North American Mesoscale (NAM) model on the 218-grid (~12 km grid spacing) is obtained from the NOAA National Operational Model Archive and Distribution System (NOMADS). The operational NAM model is run four times a day (0000 0600 1200, and 1800 UTC) and forecasts out to 84 hours, at three hour intervals. The NAM runs operationally with a WRF dynamical solver referred to as the WRF-NMM (Nonhydrostatic Mesoscale Model). There are differences in model set-up such as the horizontal and vertical grid spacing, but most physics options are the same except the microphysics and radiation schemes. The operational NAM uses the same boundary layer, surface layer, land-surface layer, and cumulus physics options that is applied to the WRF runs in this analysis.

Model output from NAM and WRF are compared to observations from several buoy stations during May and June 2012. The performance of both models are assessed with observations of the u- and v-winds at b-42, b-28, b-54, and b-53. The correlation coefficient is shown in Fig. 3.12 as a function of forecast hour from the start of the model simulation to 36 forecast hours out from initialization. As expected, the correlation tends to decrease over time, but the correlation coefficients vary greatly between each buoy location and differ between the models. In general, NAM and WRF are both highly correlated to observations upstream of PAPC and poorly correlated near points downstream. Low correlations coefficients ($r \sim 0.6$) are especially notable at b-53 in the SBC and quickly decline during the first 12 forecast hours in both models.

Correlation coefficients of the v-wind are notably high at b-42 and b-28 ($r \sim 0.9$). The performance of the NAM model is consistent with the output from WRF previously discussed, where the v-wind and along-shore flow are better simulated in the model than the u-wind or cross-shore flow. WRF has either similar or better correlation than NAM. The correlation of u-wind at b-28 and b-42 has a 12-hour cycle in both NAM and WRF, which may reflect influence of the initialization times. In the SBC (b-53), correlations of the u-wind for both models are similar and are generally more correlated than v-wind. WRF tends to perform slightly better than NAM in the v-wind direction at b-53, but with more variability for all forecast hours.

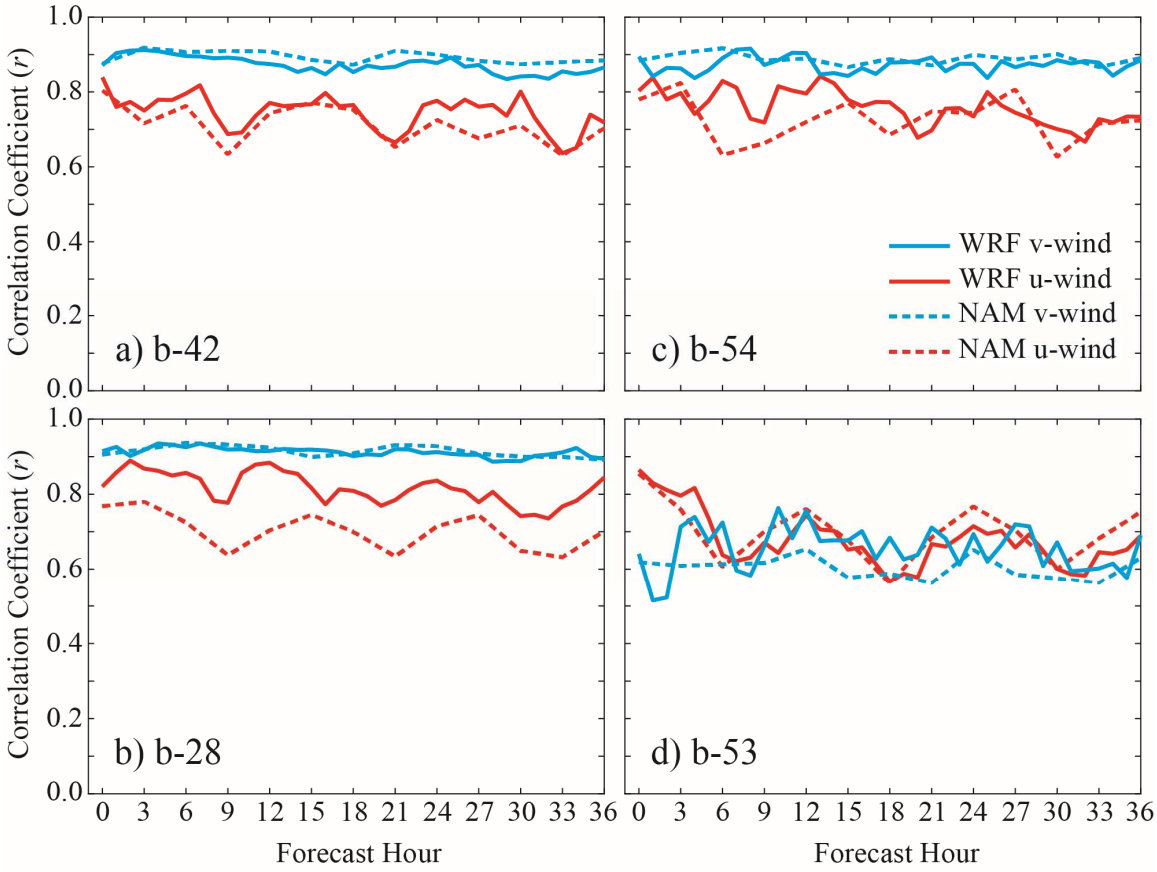

Fig. 3.12: The correlation coefficient (r) of the u- (red) and v-wind (blue) between buoy observations and model forecast hours from NAM (dashed) and WRF (solid) at (a) b-42, (b) b-28, (c) b-54, and (d) b-53.

Hodographs in Fig. 3.13 represent the diurnal cycle of the low-level wind at b-42, b-38, b-54, and b-53 during May and June 2012. The 12-23 hour forecast of the NAM during the two-month period is obtained and compiled in the same way as the WRF output. Hodographs are constructed similarly to Fig. 3.6, except the mean wind is not removed. Output from the 9-km and 3-km WRF simulations are also presented to illustrate differences from the horizontal resolution. For nearly all stations analyzed, NAM is notably different and has a clear bias in the diurnal cycle of the mean wind speed and direction. NAM tends to simulate stronger v-winds and weaker u-winds than both WRF and buoy observations at b-42, b-28, and b-54. In general, WRF performs better at simulating the diurnal cycle winds and more closely resembles the observations.

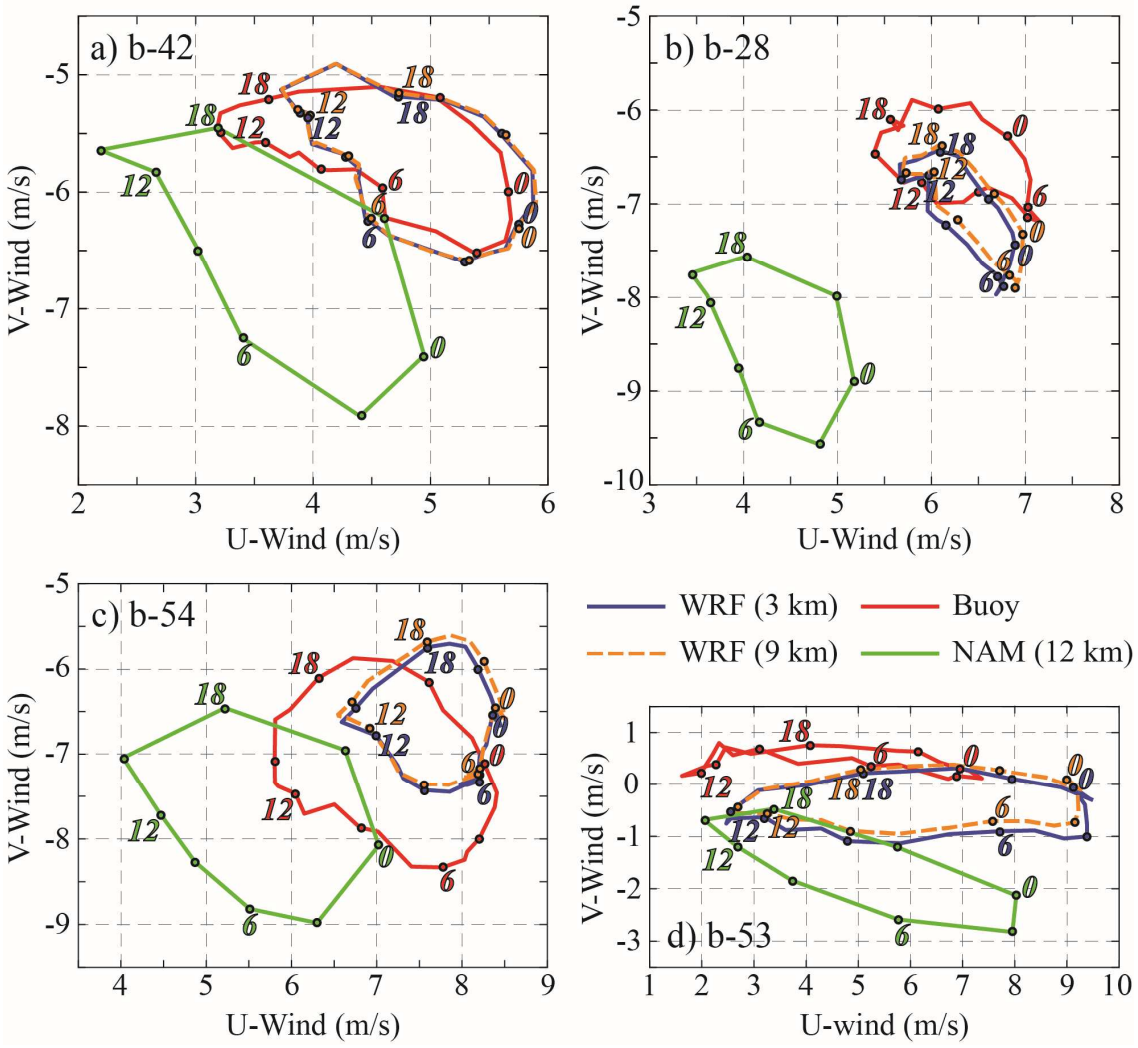

Fig. 3.13: Hodographs of the mean diurnal wind speed (m s^{-1}) during May and June 2012 comparing the 12-km NAM (green), 9-km WRF (dashed orange), and 3-km WRF (blue) simulations to buoy observations (red) at (a) b-42, (b) b-28, (c) b-54, and (d) b-53. Time of day (UTC) is labeled every 6 hours.

Differences between the 9-km and 3-km WRF simulations are minimal at all locations. Modeling of the LLJ off the coast of California conducted by Ranjha et al. (2016) showed increasing horizontal resolution from 6 km to 2 km did not improve model performance. Simulations at higher resolution increase the amount of realistic detail, but the added spatial variability at finer grid scales negatively impacted the statistics. Fig. 3.12 shows that correlations from WRF are more variable than NAM, which can be explained in part by the horizontal resolution differences between the models.

3.3) Upper-Air Analyses

Aircraft measurements from PreAMBLE are compared with WRF to investigate the differences above the surface from PAPC and into the SBC. Besides the 1200 UTC soundings at Vandenberg Air Force Base, observations of the lower atmosphere offshore of PAPC and into the SBC are rare. The upper-air analysis assesses the model inconsistencies aloft that may be related to or explain the discrepancies found at the surface. Regional composites of all aircraft soundings are constructed to provide a mean representation of the vertical structure at different areas along the coast. Model output is interpolated to the aircraft observations and the mean differences are shown. To provide more specific comparisons of the mean differences, the first two PreAMBLE flights on 16 and 18 May 2012 are used. Those two flights had similar flight patterns. The aircraft flew on an isobaric surface of ~980 hPa and conducted several sawtooth patterns between 150-900 m above mean sea level in the SBC. Strong gradients of temperature and moisture were observed at the top of the MBL, and the implications of the model and observed vertical structure on the propagation of electromagnetic microwave (EM) radiation is presented.

a. Regional Composite Soundings

In addition to isobaric legs, the aircraft performed 270 ascents and descents during PreAMBLE. Composites of the soundings in several regions highlight the differences between simulations and observations. Since the aircraft collected measurements at fine scales, the model output is linearly interpolated to the aircraft location. Four coastal regions that represent similar conditions are created (Fig. 3.14). North of 35°N is the North-Shore region that represents the upstream, along-shore flow. The PAPC region is west of 120.5°W and between 35°N and 34°N, and it largely represents the compression bulge area of the coast. The west and east regions of the SBC are separated due to differences in MBL characteristics as the flow associated with the expansion fan in the west Santa Barbara Channel (WSBC) decelerates towards the east Santa Barbara Channel (ESBC). The WSBC extends from 120.5°W to 119.9°W. The ESBC extends from 119.9°W to 119.3°W, and it represents the deeper and warmer marine layer found further into the SBC. There are 52

individual soundings within ESBC, 65 in WSBC and 72 inside the PAPC zone. Only one PreAMBLE flight on 24 May sampled data in the North-Shore region, which contains data from 19 soundings.

The vertical profiles show the observed and modeled composite temperature (°C), dew point temperature (°C), and the u- and v-wind components (m s^{-1}) from ~150-750 m above the surface. The jumps in the profiles are due to non-uniform profile depths that the aircraft flew. Dissimilarities between the model and observations are evident and varies for each region. Even in the composites, the observed temperature profiles in the North-Shore (Fig. 3.15a) and PAPC zone (Fig, 3.15d) show a well-defined inversion layer. The average depth of the MBL is marked at the base of the temperature inversion, which is ~250-300 m over both regions. The average height of the inversion in the model is roughly 100 m below observations and is not as strong nor noticeable. The simulated temperature profiles in the WSBC and ESBC regions (Fig. 3.15g and 3.15j) are nearly 2-3 °C warmer throughout the entire column than the observed temperature.

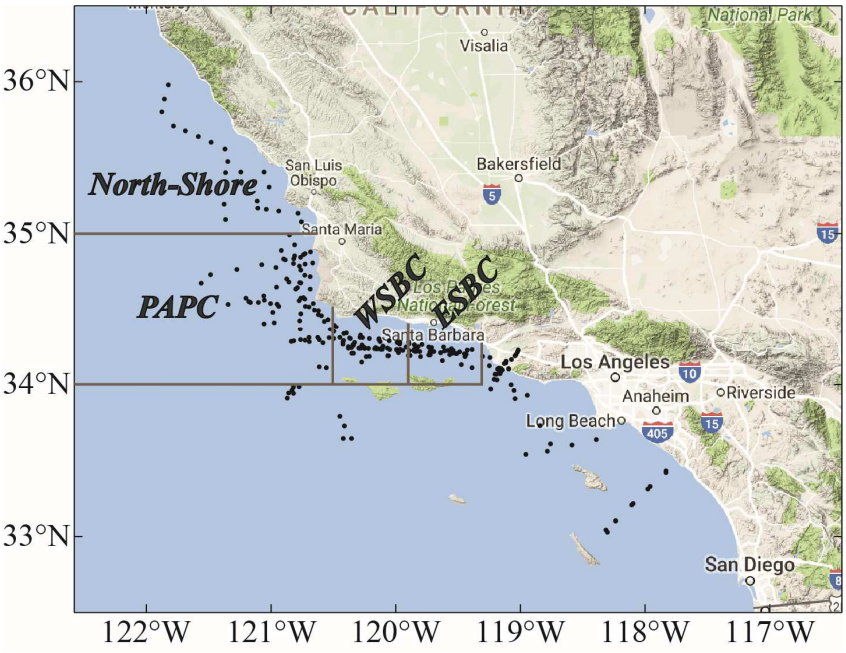

Fig. 3.14: Regions along the coast of California identified as North-Shore, PAPC, WSBC, and ESBC. Data points (black) indicate the location of individual PreAMBLE soundings outlined in each region.

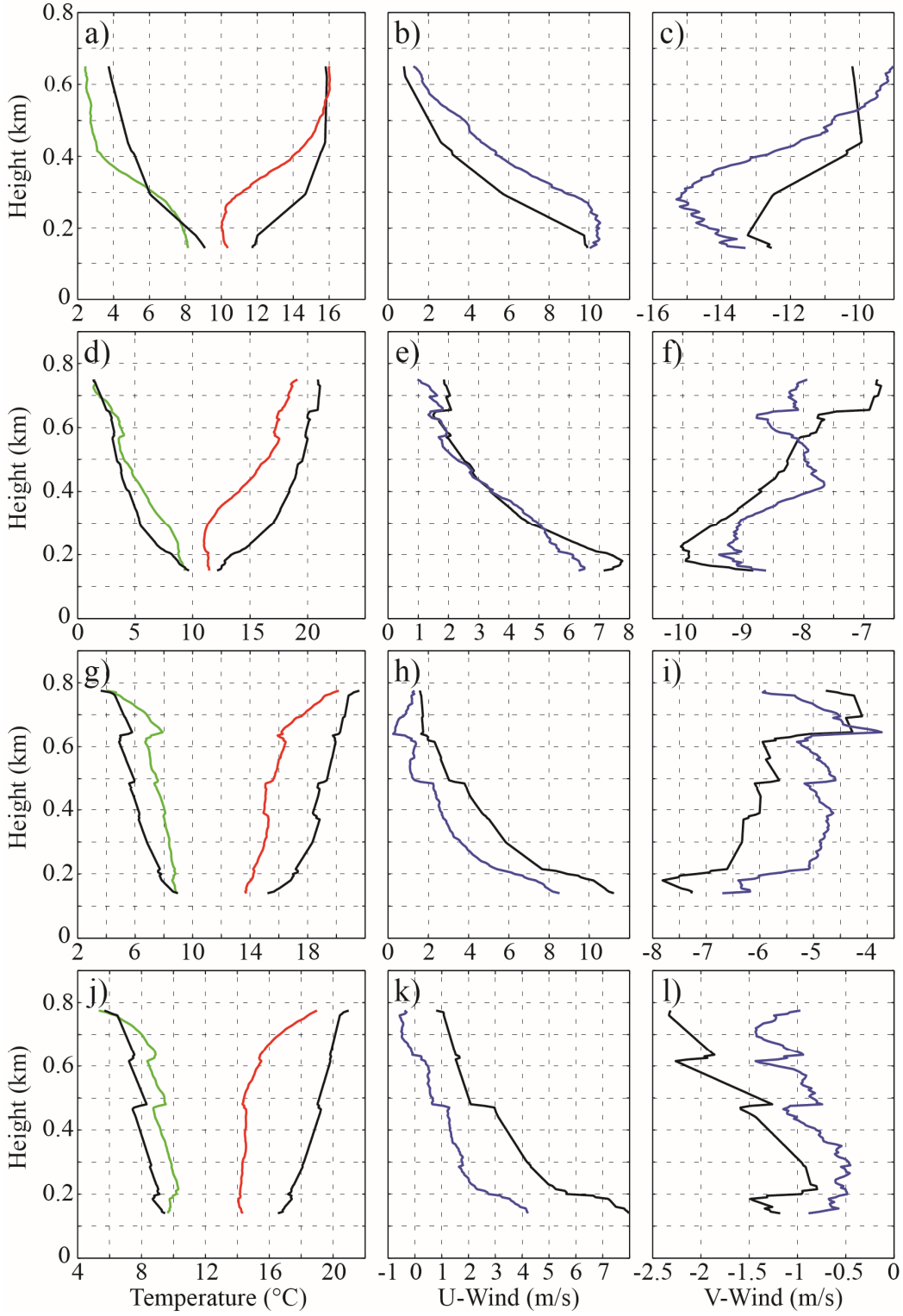

Fig. 3.15: Regional composite soundings of temperature (°C, red), dew point (°C, green), and u- and v-wind (m s^{-1}, blue) comparing aircraft data to WRF (black) in the North-Shore (a, b, c), PAPC (d, e, f), WSBC (g, h, i), and ESBC (j, k, l) regions.

The wind profiles in the North-Shore region (Fig. 3.15b and 3.15c) of both the u- and v-wind components are underestimated by the model, especially below 500 m. The maximum wind speed is observed near the top of the MBL where observations of the u- and v-wind components are 4 m s^{-1} and 2.5 m s^{-1} stronger than the simulated winds, respectively. The model better represents the u-wind in the PAPC zone (Fig. 3.15e) and shows similar magnitudes to the observations at most vertical levels, except near the height of the inversion (~200 m) where the simulated wind speed is about 1 m s^{-1} stronger (Fig. 3.15f). Further downstream into the SBC, large differences between the modeled and observed low-level flow occurs. The model tends to overestimate the magnitude of the wind across the entire channel for both WSBC (Fig. 3.15h and 3.15i) and ESBC (Fig. 3.15k and 3.15l) at all vertical levels.

b. Case Study: Description of Flights and Conditions

The regional composite soundings reveal the general model inconsistencies including a bias for warmer and drier profiles, a lower MBL depth, and stronger winds. The first two research flights on 16 May 2012 (RF01) and 18 May 2012 (RF02) provide two examples that are consistent with the composite biases. Prior work has used other research flights to investigate specific aspects of the MBL adjustment around PAPC. Rahn et al. (2013, RF03) used the precise measurements to compare the actual atmospheric response to what would be expected under an idealized scenario (channel flow analogy and Bernoulli's equation for inviscid flow), which explained most of the response. Differences were attributed to factors such as the change of inversion layer thickness or thermal gradients above the MBL. Parish et al. (2014, RF04) presented a case where the transition was strongly influenced by offshore flow. Rahn et al. (2014, RF10) revealed how easterly flow in the SBC interacted with strong northwesterly flow from north of Point Conception. Conclusions were based on observations, and results from a suite of numerical simulations for that day was shown to give poor results. Parish et al. (2016a, RF14) modeled the expansion fan and used D-value cross sections from the aircraft and simulation to assess the vertical profile of the horizontal PGF. D-values are the deviations of actual height above sea level from the U.S. Standard Atmosphere, which effectively removes the vertical component of the PGF,

thereby allowing direct visualization of the horizontal pressure gradient (Parish et al. 2016b). Near Point Buchon on 24 May 2012, a particularly windy day, Rahn et al. (2016, RF05) found evidence that Kelvin-Helmholtz instability was responsible for creating a secondary well-mixed layer above the MBL.

This work expands the number of case studies by investigating the first two research flights of PreAMBLE with a focus on the model results. These case studies illustrate the main features in the lower atmosphere near PAPC and highlight the model weaknesses. First, the heights on an isobaric surface and the corresponding PGF as well as vertical soundings are assessed. Then, a modified refractivity index is calculated from the model and observations to highlight one important implication. At the top of the MBL, strong vertical gradients of temperature and moisture can influence the propagation of electromagnetic radiation and impact communication and surface radars (Haack and Burk 2000). Atmospheric ducting can occur in shallow inversion layers that have large density changes, which can horizontally channel propagating waves and bend the signal back toward the surface.

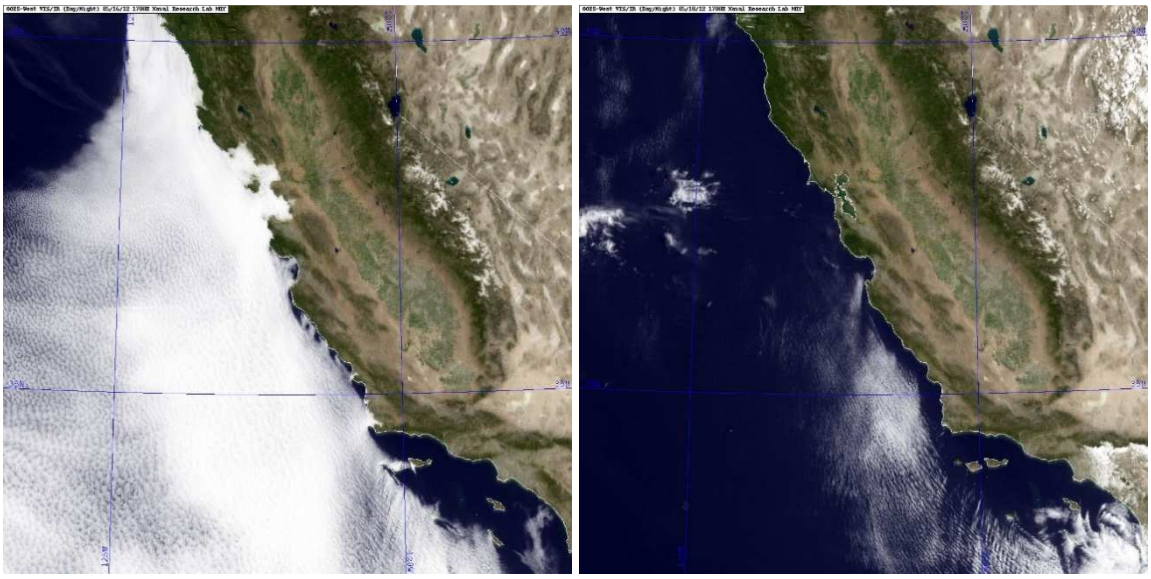

Fig. 3.16: Visible satellite images from the Geostationary Operational Environmental Satellite (GOES 15) at 1700 UTC on (left) 16 May 2012 and (right) 18 May 2012 from the Naval Research Laboratory (https://www.nrlmry.navy.mil/NEXSAT.html).

The synoptic-scale atmospheric conditions during RF01 and RF02 are typical for late spring and are similar to Fig. 1.2. A surface anticyclone was centered about 1000 km west of California and a thermal low was over the desert southwest. A relatively strong PGF drove a northerly wind along the shore. Large-scale subsidence was associated with a well-defined 500-hPa ridge over California and helped maintain a strong temperature inversion above the cool MBL. Visible satellite images from the Geostationary Operational Environmental Satellite (GOES 15) on 16 and 18 May 2012 at 1700 UTC (1000 PDT) shows more expansive cloud coverage on 16 May than on 18 May (Fig. 3.16). A sharp gradient from clear to cloudy conditions exists during both days on the western edge of the SBC and southeast of PAPC. Strong winds are observed to the north and upstream of PAPC for both days. The mean daily wind speed at b-54, located offshore of PAPC is 13.8 m s^{-1} and 12.0 m s^{-1} on 16 and 18 May 2012, respectively. Due to a strong coastal jet ($F_r > 1$), an expansion fan in the lee of PAPC and a compression bulge upstream of PAPC are expected. The sharp cloud edge is likely a result of the terrain-induced hydraulic response of the low-level flow. A hydraulic response (compression bulge/expansion fan) near coastal points is supported by the satellite observations on during RF01.

i) Isobaric and Sounding Analyses

The flight strategy for RF01 and RF02 was to spend most of the time mapping the height of an isobaric surface (~980 hPa) in the SBC and around PAPC, but a few sawtooth patterns were also flown. Isobaric maps are linearly interpolated between aircraft legs. Isobaric measurements were obtained between 1516-1803 UTC (0816-1103 PDT) during RF01 on 16 May 2012 (Fig 3.17a), and between 1452-1752 UTC (0752-1052 PDT) during RF02 on 18 May 2012 (Fig. 3.18a). The observed heights from RF01 and RF02 are compared to the simulated heights in WRF from the 17-hour forecast valid 1700 UTC for both 16 and 18 May 2012.

During RF01, the 980-hPa isobaric surface slopes downward into the SBC and the height decreases 9.0 m over 55 km from b-54 to b-53 (Fig. 3.17a). The isobaric surface from WRF has a greater decrease of 14.2 m over the same distance (Fig. 3.17b). The PGF is primarily directed from west to east and is related to the slope of the isobaric surface

($\Delta H/\Delta x$), which is 0.16 m km^{-1} and 0.26 m km^{-1} for the observations and WRF, respectively. Likewise, the modeled isobaric field during RF02 on 18 May 2012 (Fig. 3.18b) has a height change of 11.4 m ($\Delta H/\Delta x$ = 0.21 m km^{-1}), which is also greater than the observed isobaric height change of 8.4 m ($\Delta H/\Delta x$ = 0.15 m km^{-1}). The slope of the 980-hPa isobaric surface between b-54 and b-53 is greater in the simulations for both cases, which implies greater forcing in the model than in the observations. The 980-hPa isobaric maps indicate the heights from the model are 20-30 m below the heights from the observations during RF01 along much of the coastline at 980 hPa. During RF02 the observed heights are ~30 m less than the model. However, a uniform model bias does not impact the gradient.

The isobaric height, wind, and temperature of an individual flight leg (L4) during RF01 that was flown from northeast to southwest in the SBC from 1535 to 1543 UTC (0835 to 0843 PDT) is shown in Fig. 3.19. The mean wind speed over this leg is greatly overestimated by the model with a mean magnitude of 11.7 m s^{-1} compared to the observed mean wind speed of 4.6 m s^{-1}. In both the u- and v-components the model is stronger in magnitude for the entire leg. Near the coast in the SBC, the observed u- and v- winds are weak (~1-2 m s^{-1}) for about 15 km from the initial position. Observations show a rapid increase in wind speed to the south, noticeably changing around 15-20 km into the flight leg. Farther away from the coast to the south, the wind speed is consistently strong and is closer in magnitude to the simulated wind speed near -10 m s^{-1} in the meridional direction and 5 m s^{-1} in the zonal direction. The observed flow is weaker in the north likely due to the influence of coastal topography and its downstream impact on the low-level flow in the immediate lee of PAPC. Slower winds and the abrupt gradient in the observed wind speed is missed by the model. This change of wind speed is not well-represented in the model except for a much weaker wind speed transition closer to the coast within the first 5 km of the flight leg. The stronger winds in the model may be associated with the model's representation of the coastal topography and little terrain blocking north of the SBC.

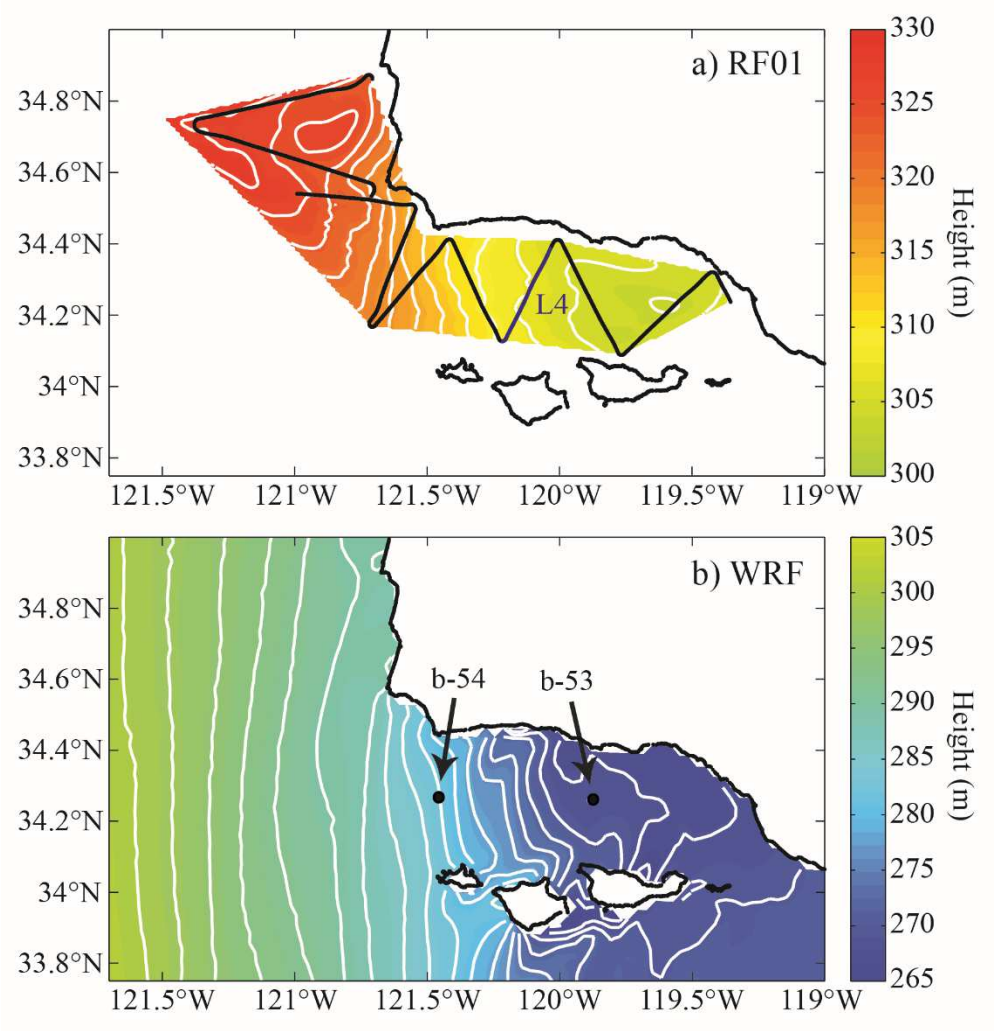

Fig. 3.17: Height of the 980 hPa isobaric surface (contoured every 2 m and color filled) from (a) RF01 observations at 1516-1803 UTC 16 May 2012 and (b) the WRF 17-hour forecast valid 1700 UTC 16 May 2012. The position of isobaric leg 4 (L4) is labeled along the flight track of RF01 (black) shown in (a), and the positions of b-54 and b-53 are marked in (b).

Isobaric heights in Fig. 3.19a indicate a stronger gradient in the model with lower heights towards the northeast. The heights in the model increase more than 8 m over the span of the 35-km flight leg whereas the observed heights increase only 2 m. The temperature in the model is between 25-30°C for the first half of the leg, which is nearly 10°C warmer than the observed temperatures in Fig. 3.19d.

Large differences also exist in the moisture and vertical motion along this flight leg (figure not shown). Observations of vertical motion are more variable than the model, but are mostly positive with a mean of 0.24 m s^{-1}. The mean simulated vertical motion for the entire flight leg is -0.06 m s^{-1}. Relative humidity is strikingly different between the model and observations. During the first 20-25 m of the flight leg, relative humidity in the observations is between 60-70%. For this same area, the model has a relative humidity between 15-25%. Observations show the relatively humidity decreasing to 30% and approaches the modeled relative humidity at 25-35 km into the flight leg.

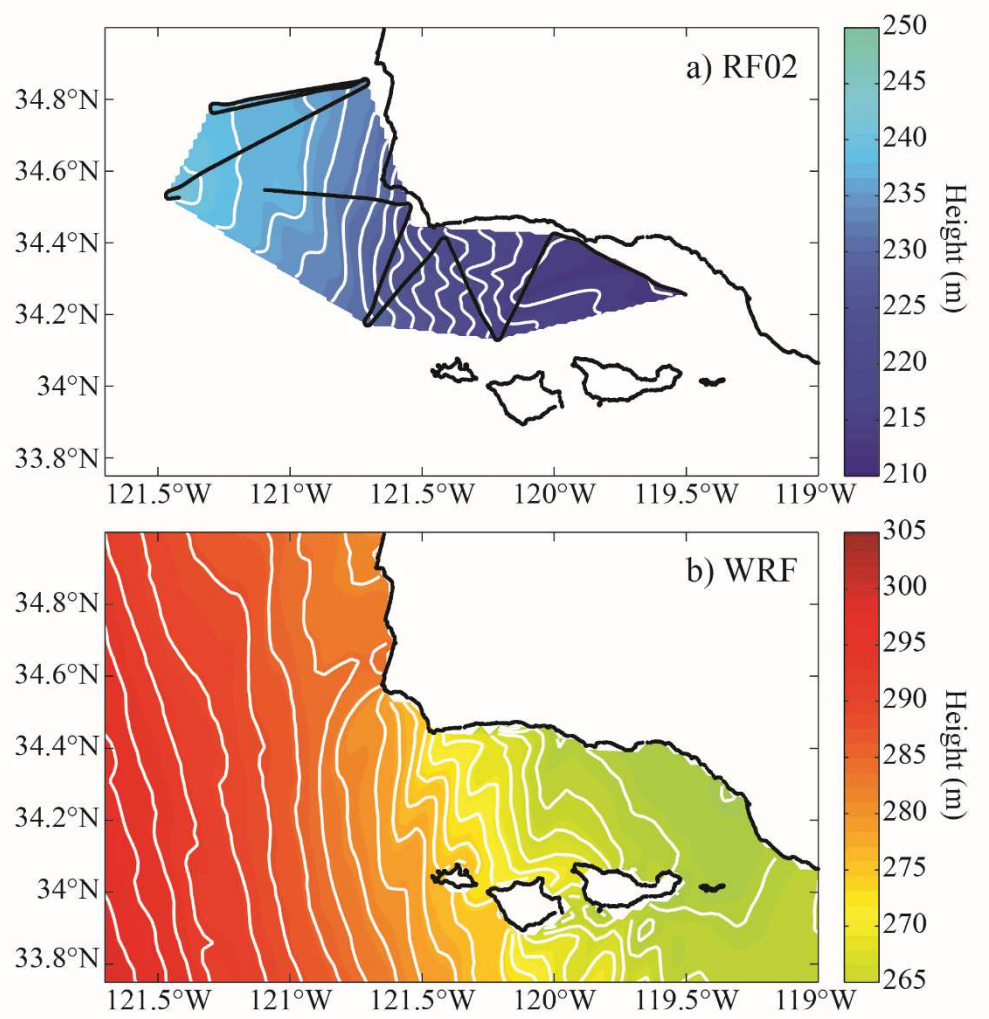

Fig. 3.18: As in Fig. 3.17, but for (a) RF02 at 1452-1752 UTC 18 May 2012 and (b) the WRF 17-hour forecast valid 1700 UTC 18 May 2012.

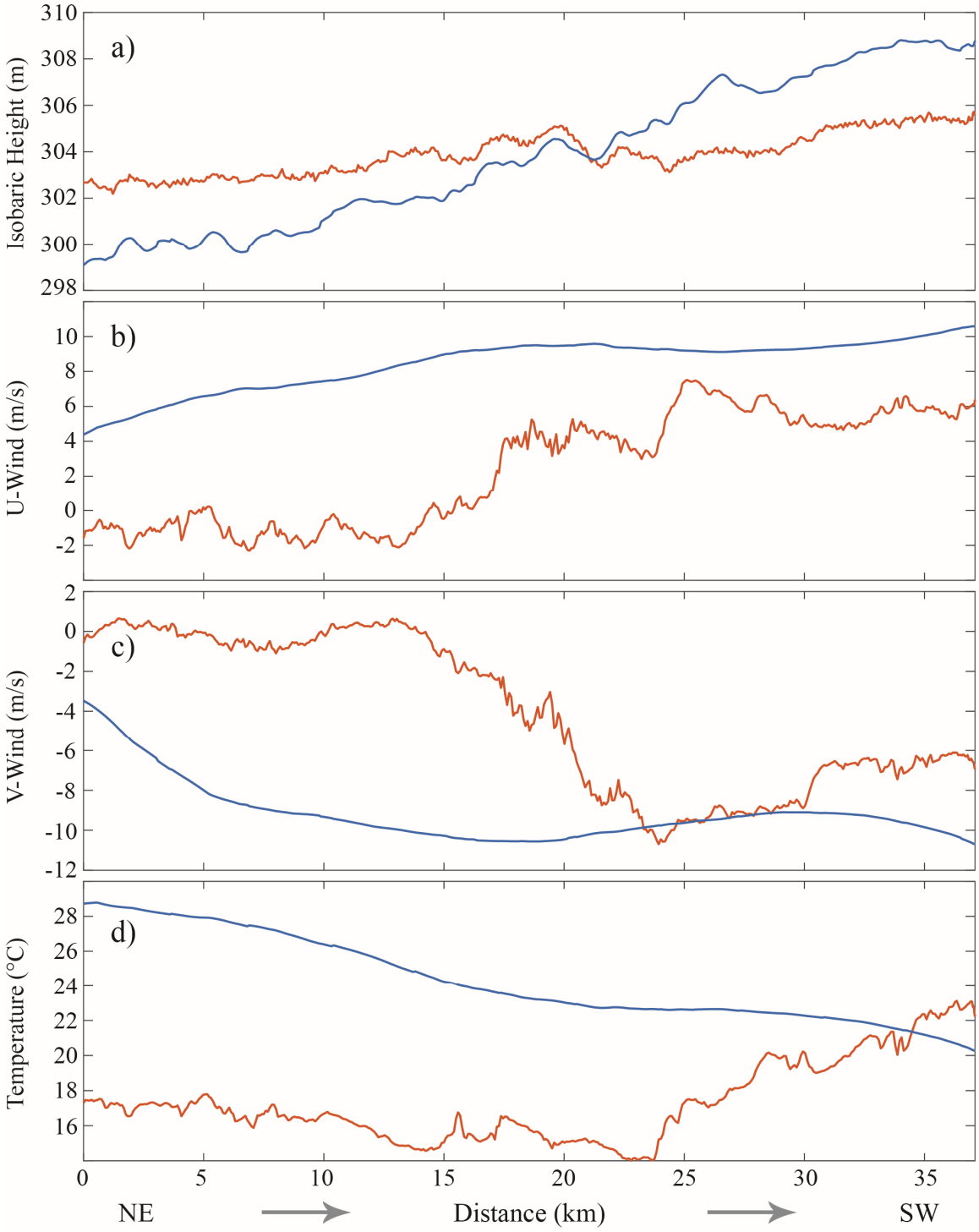

Fig. 3.19: The 980 hPa (a) isobaric height (m), (b) u-wind (m s^{-1}), (c) v-wind (m s^{-1}), and (d) temperature (°C) for RF01 isobaric leg 4 (L4) at 1535-1543 UTC (red) and the WRF 16-hour forecast valid 1600 UTC 16 May 2012 (blue). Refer to Fig. 3.17a for the location of isobaric leg 4 (L4) from RF01.

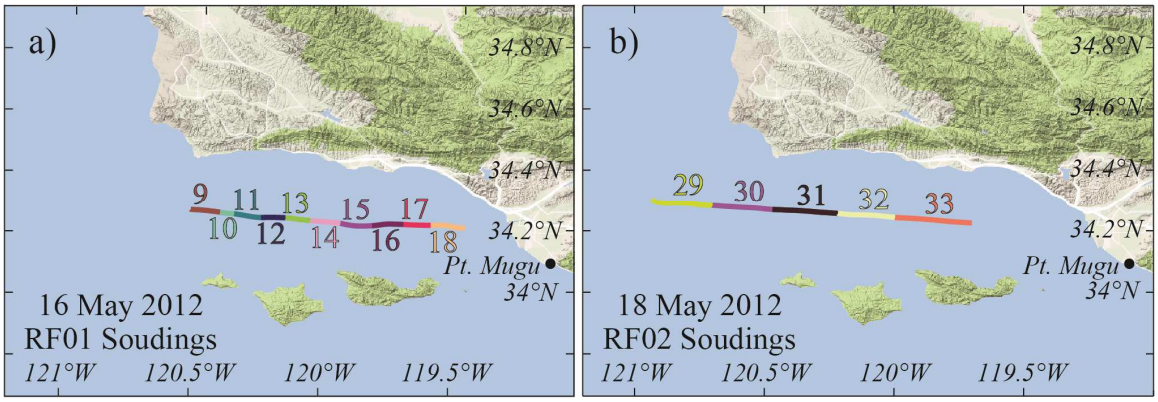

Fig. 3.20: Flight track of individual soundings (numbered and color coded) from the sawtooth pattern conducted in the SBC during (a) RF01 on 16 May 2012 from 1818-1844 UTC and (b) RF02 on 18 May 2012 from 1719-1736 UTC.

These considerable differences between the aircraft and model output reveal the model's inaccurate representation of the observed atmospheric conditions in the SBC. Along this isobaric flight track, the model is much warmer and drier with downward vertical motion, but the observations show relatively cool and moist air with upward vertical motion. This difference suggests the height of the observed isobaric surface is within the MBL whereas the same isobaric surface lies above the MBL in the model.

At the end of RF01 and RF02, the aircraft flew a series of soundings in a sawtooth pattern to measure the vertical structure in the SBC before landing at Pt. Mugu (Fig. 3.20). Cross sections of potential temperature, u- and v-wind components, and relative humidity are constructed by smoothing and then linearly interpolating the measurements. The MBL depth and the strength of the capping inversion can be interpreted from these cross sections. Aircraft observations are compared to the 18-hour WRF forecast valid at 1800 UTC for both RF01 on 16 May 2012 and RF02 on 18 May 2012.

On 16 May (Fig. 3.21), the model shows a layer of tightly-packed isentropes that slope downward from the western edge to the center of the cross section, representing a strong temperature inversion above a MBL that thins considerably as the near-surface flow enters the SBC. This is consistent with an expansion fan. Observed isentropes have more noise in part due to interpolation, but there are several noticeable differences with the simulation. Similar to the model, in the far west region the isentropes are tightly packed and in the

lowest layers the isentropes slope down towards the surface. Unlike the model, the observations show a stable layer around 300-350 m over the entire cross section with much weaker stability than the model below that layer. Strong wind in the zonal direction is confined within the MBL of the model, whereas observations show much weaker zonal winds. Similarly, the v-wind is overestimated by the model for nearly the entire vertical column of the cross-section. Observations indicate relative humidity greater than 50% below 300 m across the entire cross section. The model shows a well-defined moisture gradient with a much drier atmosphere aloft, with relative humidity less than 30% above 200 m. The height of this strong moisture gradient corresponds to the same height of the thermal gradient. The strong temperature and moisture gradient supports a well-defined inversion layer in the model. This is not the case in the observations where the temperature and moisture profiles indicate a deep well-mixed MBL.

The mean isobaric height at 980 hPa of leg 4 in the SBC is 272.8 m and 303.9 m the model and observations, respectively. The cross-sections indicate that the MBL in the model was below the mean isobaric height of leg 4. The model simulates a single, strong inversion layer above a shallow MBL, which is consistent with a strong northerly wind aloft that advects warm continental air over the MBL and is associated with lee subsidence. The stronger simulated northerly wind in the SBC extends to the coast (Fig. 3.21).

The observed potential temperature from RF02 on 18 May (Fig. 3.22) has a strong gradient in the west at the top of a well-mixed MBL near 500 m. To the east, the thermal gradient becomes more diffuse and the height of MBL top becomes less pronounced. A stable layer near 600 m exists throughout the cross section, but below 600 m isentropes slope downward to the east. The model simulates a well-defined MBL sloping down from west to east, but the entire cross section of isentropes slopes downwards without a more level distribution of isentropes around 600 m. Both wind components are again overestimated, especially below 200 m.

For the composites, these two flights, and other individual flights not shown, the observations indicate that after the low-level flow enters the SBC as an expansion fan, it encounters a deeper, slightly warmer moist layer that is separated from the free troposphere by a temperature inversion around 300-600 m. In contrast, the model almost always

simulates an exaggerated expansion fan with a temperature inversion that extends over a deeper layer and a stronger flow that penetrates further east into the SBC than what is observed. This result is consistent with greater simulated zonal wind speeds at the buoys in the SBC. Model results have been the basis for the conceptual model of flow near PAPC, but the differences between model and observations reveal weaknesses in the conventional conceptual model. Similar to what is shown in Fig. 3.21b, Dorman and Koračin (2008) depict a continuous transition of the cool MBL upstream of PAPC into the expansion fan in the SBC and then this layer deepens further east as the flow transitions back to subcritical (cf. their Fig. 7). This new observational data in the SBC from PreAMBLE reveals the lowest layer associated with the expansion fan is confined to a thin layer at the surface under a slightly warmer and deeper layer found in the California bight. Above the slightly warmer layer is a marked inversion separating it from the free troposphere above. Typically, the warm layer is observed when easterly winds occur overnight in the eastern half of the SBC. In fact, the composite of PreAMBLE soundings in ESBC shows a temperature inversion and easterly flow above 600 m (Fig. 3.15k). This warm layer is above the lowest cool layer associated with the expansion fan, which erodes eastward as it encounters warmer SSTs, increasing the sensible heat flux and low-level mixing. As shown in the composite soundings, in these two cases, and in other cases not shown, the comparison between the model and observations reveals that the model does not correctly capture the subtle layering within the SBC. Thus, the model overestimates the zonal wind in the SBC, which is reflected clearly in the surface observations at b-53. The modeled surface wind is tied to the exaggerated portrayal of an expansion fan that extends too far into the SBC, which can have a profound impact on the representation of wind stress on the ocean surface and the profiles of temperature and humidity in the SBC.

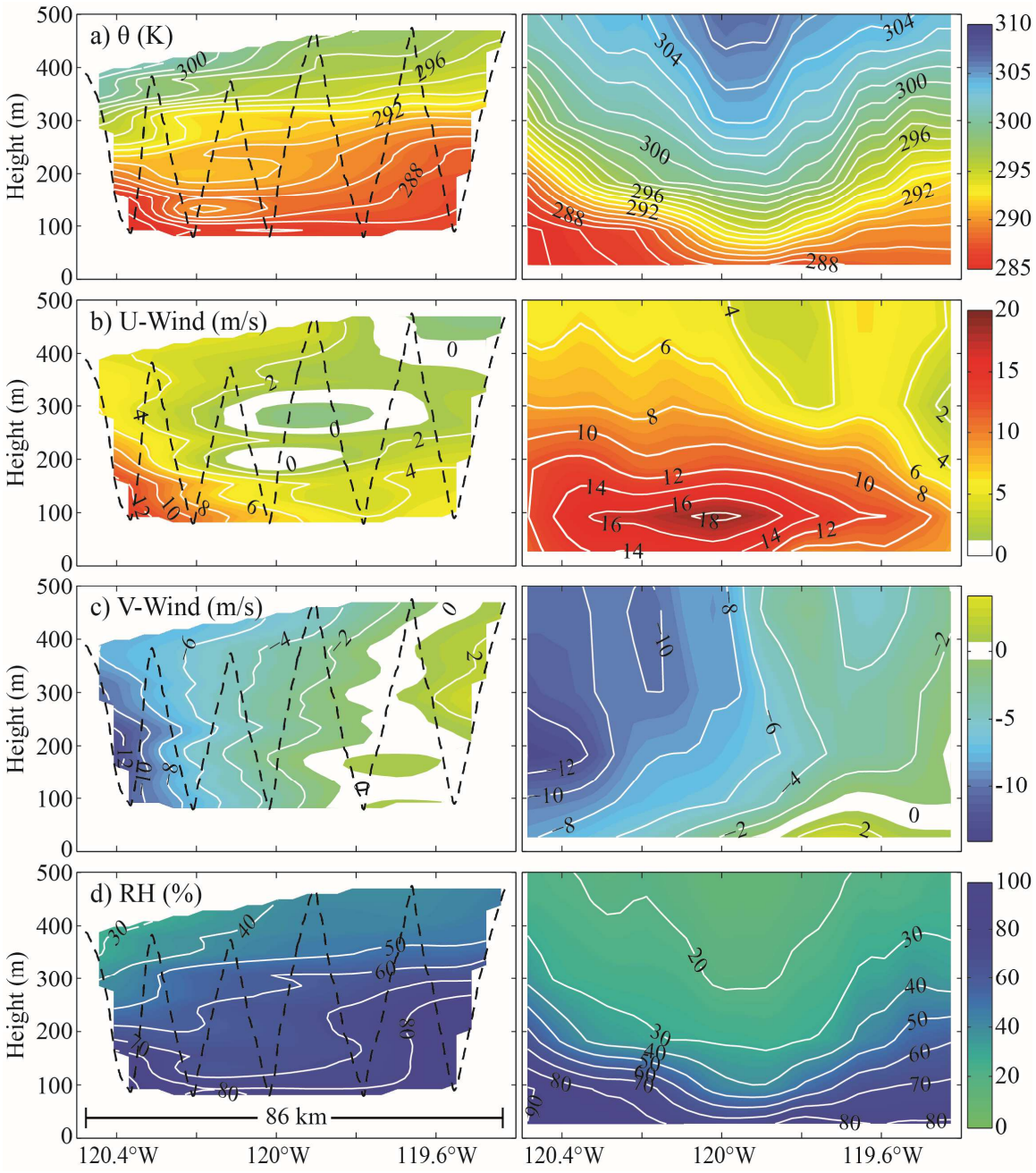

Fig. 3.21: Sawtooth leg from RF01 (dashed line) in the SBC from 1818-1836 UTC on 16 May 2012 showing (a) potential temperature (K), (b) u-wind (m s^{-1}), (c) v-wind (m s^{-1}), and (d) relative humidity (%). Aircraft observations (left) are compared to WRF output from the 18-hour forecast valid 1800 UTC 16 May 2012 (right). The horizontal distance of the flight leg is shown at the bottom right. Refer to Fig. 3.20a for flight track.

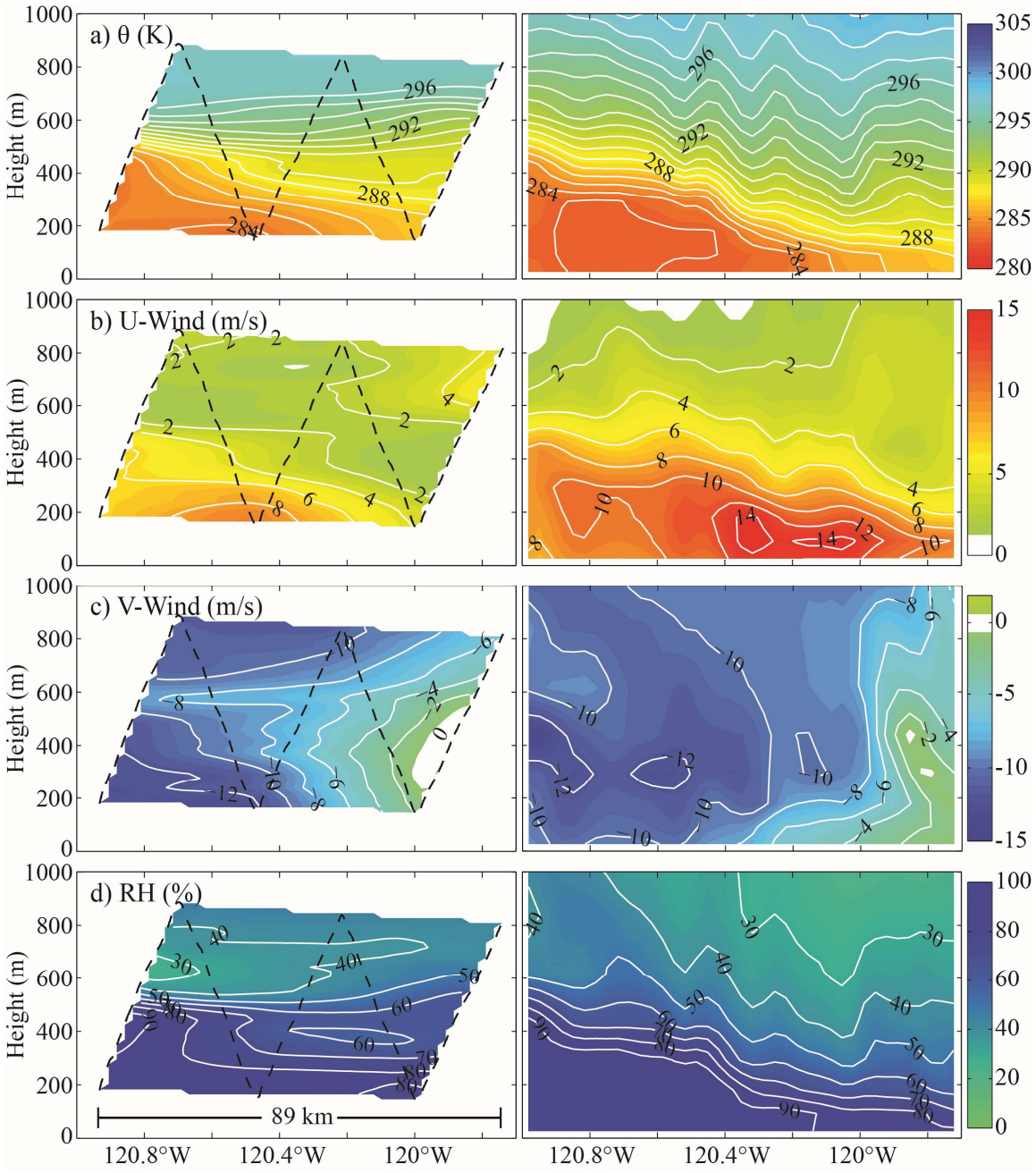

Fig. 3.22: As in Fig. 3.21, but for RF02 from 1719-1736 UTC on 18 May 2012 compared to WRF from the 17-hour forecast valid 1700 UTC 18 May 2012. Refer to Fig. 3.20b for flight track.

ii) Influence on Atmospheric Refractivity

Numerical weather prediction is used by national defense agencies around the world to support military intelligence and operations. High resolution atmospheric models are needed for strategic information about radar performance, communication signals, and surveillance purposes (Brooks et al. 1999; Atkinson and Zhu 2006; Haack et al. 2010). Agencies such as the Marine Meteorology Division of the U.S. Naval Research Laboratory in Monterey, CA and the Vandenberg Air Force Base and Space Launch located near PAPC are particularly concerned with atmospheric refraction and its effect on their operations, especially radar and communication signals, which is a concern for national security (Burk and Thompson 1997; Brooks et al. 1999; Wang et al. 2012). Consequently, it is imperative to recognize the deficiencies of numerical weather prediction models and the impacts associated with electromagnetic radiation (EM) propagation in the atmosphere.

Large gradients of temperature and moisture that occur at the top of the MBL along the coast of California influence EM propagation emitted at a low elevation angle. Under the right conditions, EM radiation can become bent enough by atmospheric refraction that it can bend back towards the surface and become trapped in a layer, which is known as atmospheric ducting (Haack and Burk 2001). Ducting layers are typically found near the base of the inversion. The height and intensity of atmospheric ducting layers are influenced by changes along the coastline, emphasizing the importance of testing the model's ability to simulate refractivity. The capacity for numerical weather prediction models to accurately represent and forecast refractivity profiles poses a difficult, yet important challenge to address (Burk and Thompson 1997; Atkinson and Zhu 2005; Zhao et al. 2016).

Atmospheric refractivity depends on the gradient of the index of refraction, which is a function of air density. An expression for the index of refraction (n) with radiation at microwave frequencies can be approximated as:

$$N = (n - 1) \times 10^6 = \frac{77.6}{T}\left(p + 4810\frac{e}{T}\right), \qquad (3.10)$$

where N is the atmospheric refractivity (dimensionless), T is the temperature (K), p is the ambient pressure (hPa), and e is the vapor pressure (hPa). A quantity related to the refractivity N that includes the effects of the curvature of the earth is approximated by:

$$M = N + \frac{z}{R_e \times 10^{-6}} \tag{3.11}$$

$$M = N + 0.157z\,, \tag{3.12}$$

where M is the modified refractivity (M units), z is the altitude above mean sea level (m), and R_e is the radius of the earth (m). An advantage of using M instead of N is that negative vertical gradients of M ($dM/dz < 0$) are layers in which atmospheric ducting conditions exist (i.e., where the temperature increases with height and/or vapor pressure decreases with height, Basha et al. 2013). For that reason, a negative slope of M is easily identified in profiles and are referred to as microwave trapping layers depending on the angle of incidence of the propagation into the layer (Burk and Thompson 1997). The effects of atmospheric refractive conditions and anomalous propagation of EM waves can lead to large errors in target detection and motion estimates (Thompson and Haack 2011).

The depth of an elevated duct ΔD is defined in the region where $M > M_{min}$ (Fig. 3.23a), which is bounded at the top by the local refractivity minimum M_{min} and at the bottom by Z_d where $M_{min} = M$. If M_{min} lies above the surface and $M > M_{min}$ at all levels below, the base of the duct is at the surface and is referred to as a surface-based duct (Fig. 3.23b). Surface ducting conditions are of interest since radars and other transmitters/receivers at the surface are affected more by anomalous propagation when the base of the duct occurs at the surface. Evaporation ducts are essentially surface-based ducts, but only within a few tens of meters above the surface and commonly occur over open bodies of water because of a large humidity gradient (Brooks et al. 1999). The strength and duration of evaporation ducts varies greatly by location, season, and time of day.

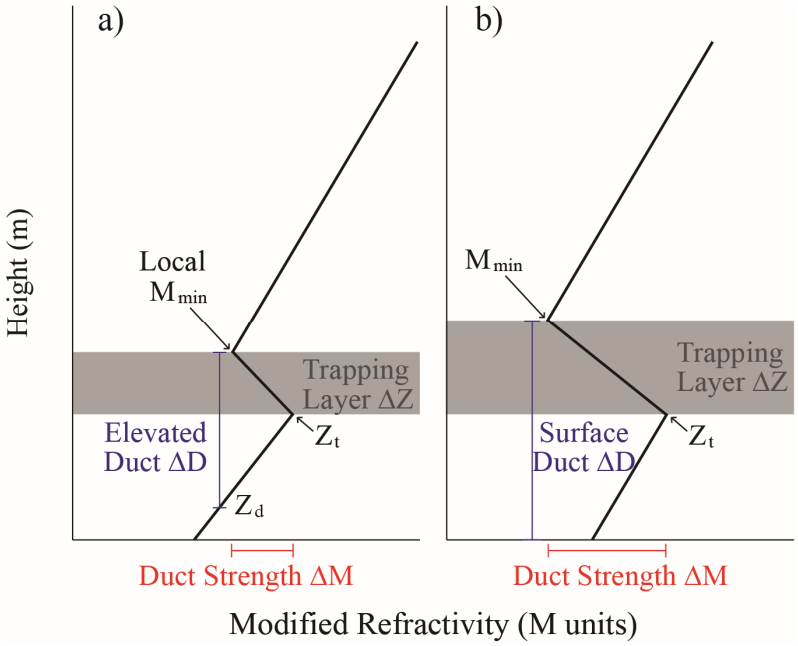

Fig. 3.23: Idealized vertical profiles of modified refractivity illustrating an (a) elevated duct and (b) surface-based duct. The grey area represents the trapping layer ($dM/dz < 0$) and lies below the (local) M_{min} and above the trapping layer base height Z_t for surface-based (elevated) ducts. Note that the duct depth ΔD is greater than the trapping layer depth ΔZ since the duct base height extends below the trapping layer base height $Z_d < Z_t$ (adapted from Haack and Burk 2001).

Atmospheric ducting conditions and the height of trapping layers are investigated in the SBC and near PAPC using aircraft observations. WRF's ability to forecast refractivity conditions is assessed by comparing its output to PreAMBLE aircraft observations by using RF01 and RF02 as the representative cases. Anomalous propagation of EM radiation occurs within elevated and surface-base ducts. However, it is not possible to distinguish whether a ducting layer is surface-based or elevated since sawtooth flight paths were flown at a minimum height near tens to hundreds of meters above the surface. The sawtooth flight path conducted on RF01 flew as low as 90 m above the surface with a depth of around 300-400 m. Vertical profiles of M in the SBC for RF01 are shown in Fig. 3.24. The individual soundings are in consecutive order from sounding 9-18 as the aircraft flew west to east across the channel (refer to Fig. 3.20 for the locations and times). Trapping layers are highlighted for both the model and observations for each sounding.

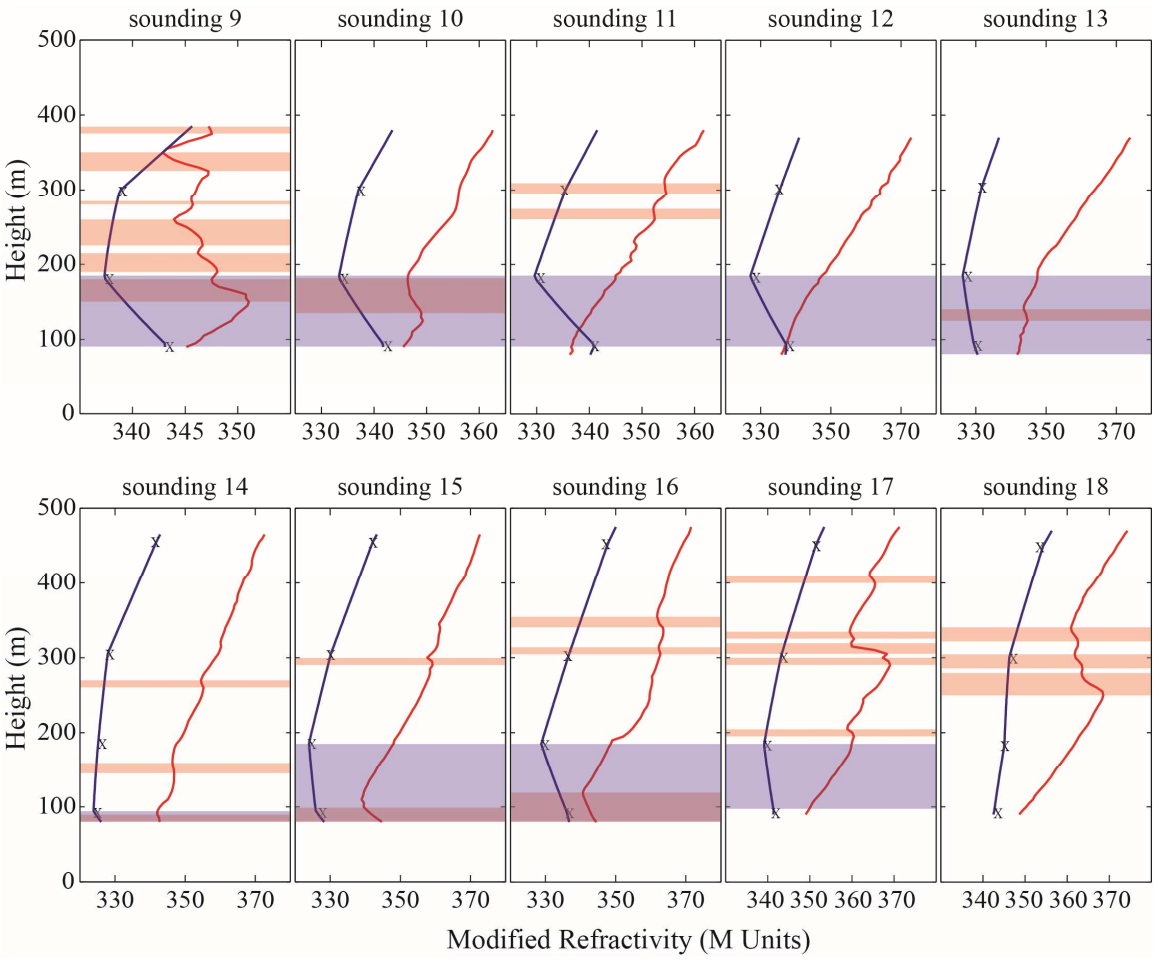

Fig. 3.24: Vertical profiles of the observed (red) and modeled (blue) modified refractivity from RF01 soundings 9-18 (labeled at the top) and the WRF 18-hour forecast valid 1800 UTC 16 May 2012. The "X" marks the model level heights in WRF. Areas of $dM/dz < 0$ are shaded in the observed (red) and modeled (blue) profiles.

The model shows a relatively large trapping layer depth of ~100 m across most of the SBC from roughly 100-200m above the surface. A vertical cross-section of the modeled trapping layer, where $dM/dz < 0$ is taken from the WRF 18-hour forecast valid 1800 UTC 16 May 2012 (Fig. 3.25). The cross-section from WRF reveals the vertical structure from the surface to 500 m above and provides an additional perspective of the trapping layers modeled through the SBC. Surface-based ducting exists in WRF between 120.1°W to 119.7°W longitude, which corresponds to the locations from sounding 13-16. The ducting layer at the surface reaches a height of around 200 m and roughly 40 km wide.

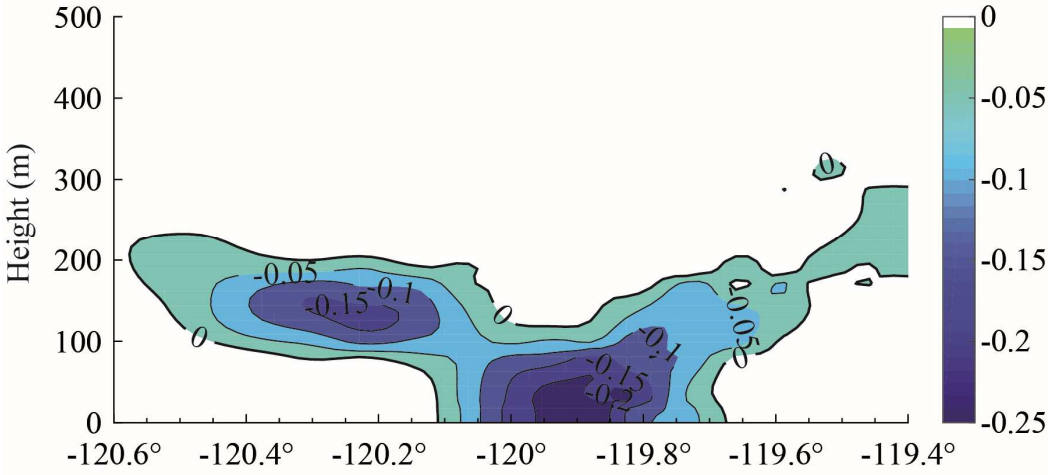

Fig. 3.25: Cross-section of ($dM/dz < 0$) the trapping layer (contoured every 0.05 m^{-1} and color filled) from the WRF 18-hour forecast valid 1800 UTC 16 May 2012 along the flight path of RF01 in the SBC (refer to Fig. 3.20a for geographic location).

Due in part to higher resolution, observations show more variability in areas where negative gradients of *M* occur and the observed trapping layer depths are much less than the modeled trapping layer depths for this event. An elevated duct is observed in sounding 9 and 10 below 200 m. Although a deeper ducting layer may be apparent in sounding 9, it is not known whether this duct is elevated or surface-based since there is no aircraft data from the surface to 90 m above. Trapping layers are observed from sounding 14-16 near 100 m and from sounding 17 and 18 near 300 m. In general, the simulated trapping layers are deeper than the observed values, especially below 200 m about the region of the inversion and boundary layer height.

Vertical profiles of *M* for soundings 29-33 during RF02 are shown in Fig. 3.26. The aircraft flew over a greater depth than RF01 from 180 m to 885 m above the surface. The WRF 17-hour forecast valid 1700 UTC 18 May 2012, shows no layers with a negative gradient of *M* ($dM/dz<0$). Observations show a pronounced trapping layer in sounding 29 between 480-555 m above the surface, but only minor layers in the other soundings. The thin layers of negative reflectivity are most likely associated with turbulence, which produces fluctuations in temperature and humidity large enough to impact *M*. The main impact of the small-scale fluctuations is to enhance scatter of EM radiation, a process called troposcatter. In sounding 29 the energy would be ducted below the trapping layer base of

$Z_t = 480$ and results in a greater ducting depth than the trapping layer depth ($\Delta Z < \Delta D$). For this case, the ducting layer is clearly an elevated duct with a depth of $\Delta D = 220$ m. The ducting layer is defined at the top by the local $M_{min} = 555$ m and at the bottom by $Z_d = 335$ m. The strength of the elevated duct is $\Delta M = 17.8$ M units, which is the difference in the modified refractivity observed at the base of the trapping layer Z_t ($M = 388.4$ M units) and at the local M_{min} ($M = 370.6$ M units).

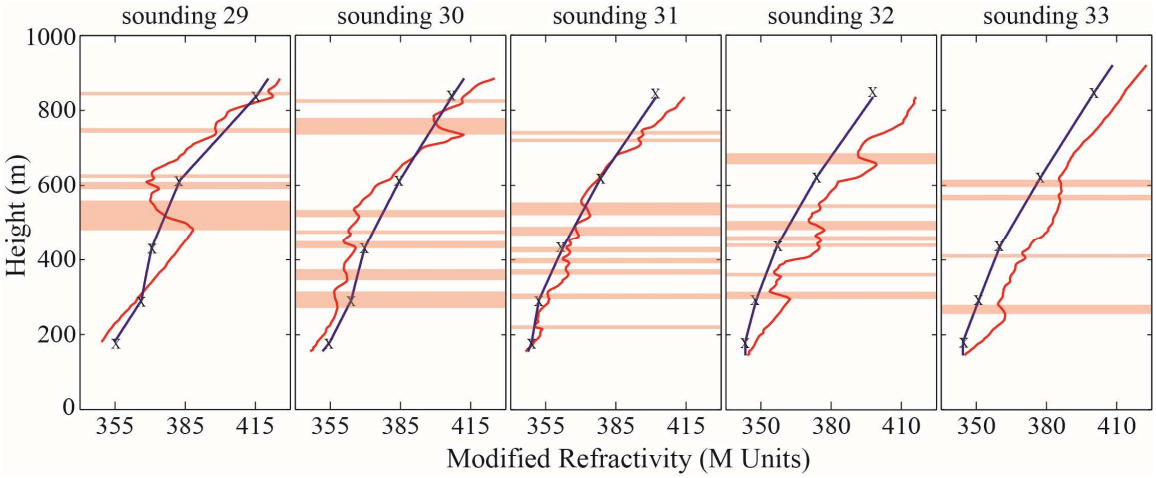

Fig. 3.26: As in Fig. 3.24, but for RF02 soundings 29-33 and the WRF 17-hour forecast valid 1700 UTC 18 May 2012.

The potential temperature θ (K), mixing ratio r (g kg^{-1}), wind speed U (m s^{-1}) and direction (deg) for sounding 29 is compared to the modified refractivity (M units) in Fig. 3.27 to show vertical structure and relationship between these atmospheric variables. Strong thermal and moisture gradients, as well as changes in wind speed and direction occur within the same vertical boundaries where $dM/dz < 0$. Although EM propagation tends to be ducted below the trapping layer and within the depth of the duct, the most abrupt changes take place at the trapping layer base height $Z_t = 480$ m, which marks the height of the inversion and top of the MBL. The simulated profiles of sounding 29 indicate a lower inversion height at 290 m for sounding 29. At this height, changes in the simulated temperature, moisture, and wind speed and direction are apparent, but the gradients are much weaker than what is observed in the vertical profiles. Therefore, the model has

difficulty in simulating trapping layers, not only for sounding 29, but for the entire flight path of RF02 across the SBC. For heights below Z_t, observations show little variability with relatively cool temperatures, high moisture content, and strong winds. Near the surface are observed means of θ = 284 K, U = 13.6 m s^{-1}, and relative humidity > 90%. Within the trapping layer and above the inversion, the temperature quickly warms, the wind speed decreases, and the atmosphere becomes much drier. Within the depth of the trapping layer $\Delta\theta$ = 7 K, ΔU = -5.9 m s^{-1}, and Δr = -2.8 g kg^{-1}.

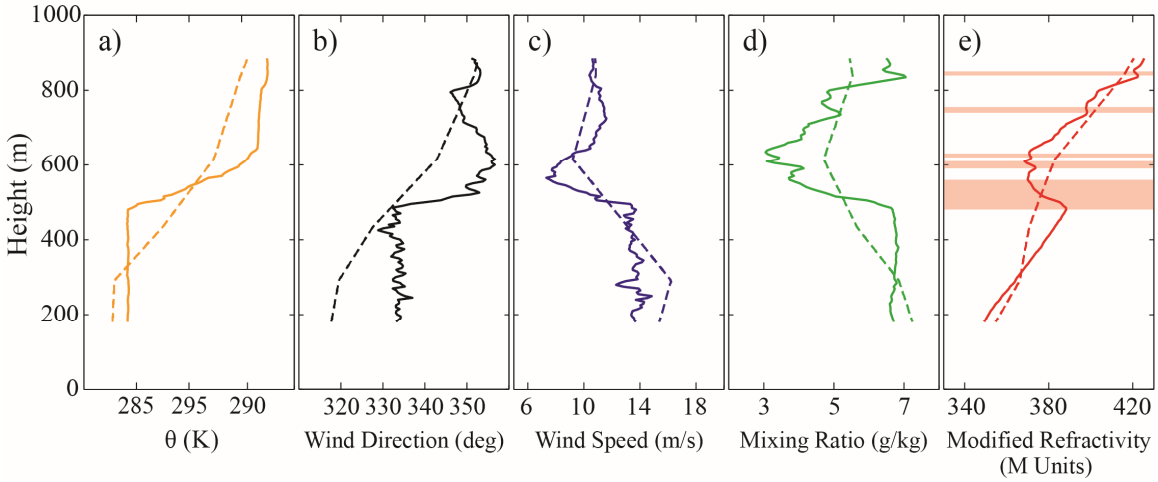

Fig. 3.27: Vertical profiles of the (a) potential temperature θ (K), (b) wind speed (m s^{-1}), (c) mixing ratio (g kg^{-1}), and (d) modified refractivity (M units). The observed profiles (solid lines) are from RF02 sounding 29 at 1719 UTC 18 May 2012 and the modeled profiles (dashed lines) are the WRF 17-hour forecast valid 1700 UTC 18 May 2012.

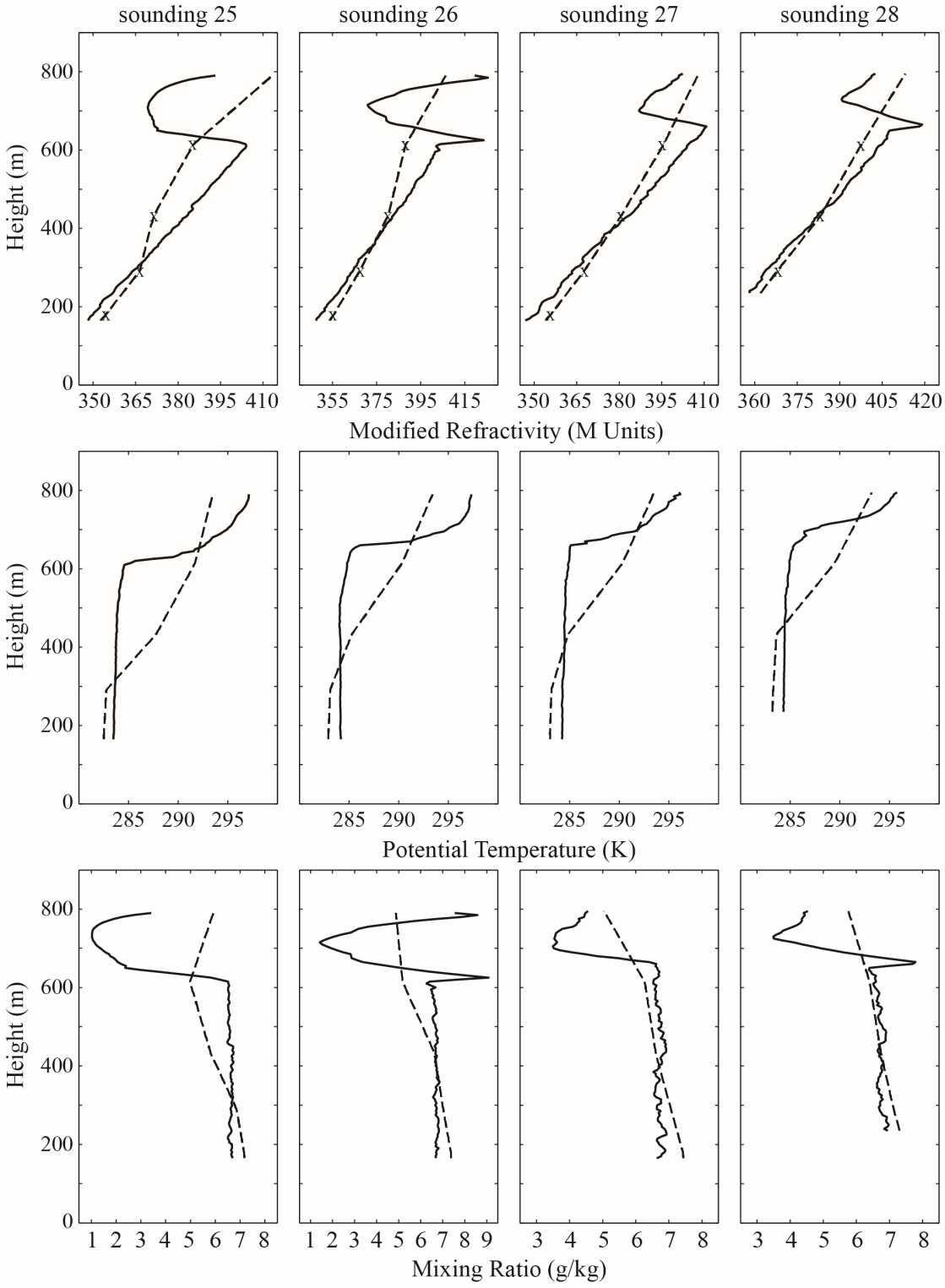

Fig. 3.28: Soundings of modified refractivity (M units), potential temperature (K), and mixing ratio (g kg^{-1}) for RF02 at 1642-1654 UTC on 18 May 2012 (solid) and the WRF 17-hour forecast valid 1700 UTC 18 May 2012 (dashed).

Strong gradients of temperature and moisture offshore of southern California lead to atmospheric trapping layers and anomalous EM propagation associated with atmospheric ducting. Aircraft observations from sounding 29 during RF02 showed a well-defined trapping layer and elevated duct at 480 m above the surface, but the simulated modified refractivity vertical structure showed no evidence of any trapping layers in the depths within the vertical column flown by the aircraft and $dM/dz > 0$ for the entire cross-section of the SBC.

During RF02, the aircraft performed a sawtooth maneuver between 200-800 m from east to west just north (upstream) of PAPC from 1642 to 1654 UTC (0942 to 0954 PDT). Soundings from aircraft observations (Fig. 3.28) show a distinct elevated duct and trapping layer $dM/dz < 0$ that is close to 100 m in depth. This negative M layer has a base height of 600 m close to the coast (sounding 25), and increases about 50 m further away from the coast (sounding 28). A comparison to the WRF simulation of the 17-hour forecast valid 1700 UTC 18 May 2012, shows no indication of a trapping layer or any layer where $dM/dz < 0$. Observed soundings of potential temperature and mixing ratio support the existence of a well-defined trapping layer with strong gradients in temperature and moisture at the same corresponding height above the surface. Large changes in the temperature and moisture profiles near 600 m also slope upward away from the coast. The atmosphere below the trapping layer is well-mixed, indicative of a typical MBL capped by warm, dry air above. The elevated duct detected by the aircraft is completely missed by the simulation.

Near the height of the trapping layer base, observations of wind speed and direction show a sharp transition marked at this boundary. Winds are out of the NNW within the MBL and shift to a more northerly direction above the MBL, which is more notable in the soundings near the coast. Subtle changes in the temperature and moisture profiles suggest the transport of warmer and drier air near 300 m. Despite these slight changes, temperature and moisture gradients in the model are not strong enough to support atmospheric ducting conditions.

Chapter Four
Summary and Conclusion

Complex coastal processes offshore of southern California are a demanding test for numerical weather prediction models. PreAMBLE data are used to investigate the lower atmosphere and to evaluate WRF. Few airborne observations have been collected near PAPC, which makes this data a valuable source of information. During PreAMBLE, it was noted that the performance of operational mesoscale models such as the 12-km NAM was poor on most days. Basic meteorological parameters such as wind speed were not consistent with model prediction and created some uncertainty for planning flights. Initially, this was attributed to the coarse resolution (~12 km grid spacing) of the NAM. Prior to this work, only a few cases were simulated with WRF and even though the model resolution was increased, the results were mixed. To better quantify the errors during PreAMBLE, WRF was ran at a 3-km grid spacing over May and June 2012. Comparison to aircraft observations still showed substantial model deficiencies. These deficiencies motivated this study to investigate model performance compared with aircraft data. Three research questions drove the analysis: (1) Where are model inconsistencies the greatest along the coast of southern California? (2) Are model errors larger under certain synoptic conditions? (3) What are the implications associated with poor model performance?

Comparison between WRF simulations and buoy observations revealed that the greatest inconsistencies of the surface winds occurred in the SBC where the model had stronger westerly winds. The model performs best in the upstream region of the coast, especially when the along-shore winds are strong. However, the model underestimates the magnitude of the surface wind both upstream and near PAPC, and there are poor correlations in the cross-shore flow. Poor model performance is more obvious in the SBC where low correlation coefficients are seen for both the u- and v-wind components.

The diurnal variability of the wind speed and direction shows the strongest winds occur during the late afternoon hours at all buoy locations, with the largest diurnal cycle occurring at b-54 near PAPC. Observations lag WRF simulations by at least three hours upstream along the coast. A possible mechanism driving the lag in the observations near Monterey

Bay is that there is typically much less morning fog/low-level cloud cover in the simulations. The absence of fog/low-cloud may lead to earlier warming over the land in the model, which would accelerate the flow sooner than reality. Future work testing the sensitivity of coastal flow acceleration to the model's ability to simulate early morning fog and cloud cover is needed to test this hypothesis. Further downstream, large differences in the diurnal cycle exist in the SBC. Kernel density distributions of the wind at b-53 show a stronger u-wind in the model. A possible mechanism for stronger winds may be a response to the model underestimating the amount of blocking that occurs as the flow encounters the high terrain over PAPC.

Model performance is linked to the strength of synoptic forcing. The model generally performs better under strong synoptic forcing when the low-level wind speed is high and the flow is well into the supercritical range ($F_r > 1$). Differences under strong and moderate forcing result in small errors upstream, but relatively large errors exist for all forcing events in the SBC. Most of the error is not linearly systematic since the unsystematic component of the *RMSE* is greater for all forcing regimes. The strength of the synoptic forcing has little influence on the winds in the SBC.

These conclusions address the first two research questions. First determining where model inconsistencies are the greatest along the coast of southern California, and then testing the dependency of model performance under certain synoptic conditions. Output from the NAM model is consistent with the results shown in WRF, and the results demonstrate higher correlation coefficients upstream than downstream. In the NAM model, there is also an overestimation of the wind in the SBC consistent with the WRF results, and therefore is indicative of an issue not only found in these WRF simulations. Identifying this model bias is important because it can make operational forecasting a challenge along the coast of southern California. Furthermore, as shown in several figures such as the time series and KDE, the wind relaxation events are particularly poorly captured by the model since WRF tends to maintain consistently stronger equatorward wind along the coast. Relaxation of the northerly wind is accompanied by a clear oceanic response near PAPC typified by poleward currents that transport the warmer waters from the SBC northward along the coast 10 to 30 km per day (Melton et al. 2009; Washburn et al. 2011). Wind

relaxation events change nutrient delivery, impact transport of larvae, and the warmer water advected northward from the SBC increases ocean stratification. An understanding of long-term trends of these events and their impact on the ecosystem is challenging but important (Washburn and McPhee-Shaw 2013). Previous studies have relied primarily on wind observations from buoys, and this work emphasizes that contemporary models such as WRF still have difficulty in capturing wind relaxation events and can even entirely miss an event such as the wind relaxation that occurred on 3 May 2012 (Fig. 3.3).

To extend the analysis above the surface, a regional composite of the entire suite of PreAMBLE sounding data was used to assess WRF output and shows large discrepancies in the lower atmosphere, especially in the SBC where the model overestimates the magnitude of the wind across the entire channel at all vertical levels. Upstream of PAPC the modeled winds are underestimated, especially within the MBL (below ~500 m). The first two PreAMBLE research flights were used to provide more specific examples of the conclusions drawn from the composites and to compare aircraft observations on an isobaric surface to the model. Results indicate the model's poor ability to accurately simulate the height of the isobaric surface. For both cases the modeled slope of the 980 hPa surface is greater, which implies greater forcing in the model than in the observations. Stronger winds in the model extend further east into the SBC than observed, which is consistent to what was found at the surface from buoy observations.

Differences between the model and observations indicated the source of the flaws to the previous conceptual model of the MBL transition from PAPC into the SBC that was based on surface observations, wind profilers over land, and model data (Dorman and Koračin 2008). Observations show two main layers in the MBL and indicate the transition of the MBL around PAPC is not as continuous as previous work depicted. A MBL ~300-600 m deep is associated with light or easterly winds exists in the SBC and is capped by a strong temperature inversion associated with subsidence in the free troposphere aloft. In the western SBC near PAPC, there is slightly cooler layer at the surface that is associated with the expansion fan and winds from the west. This lowest layer erodes as it encounters warmer SSTs towards the eastern section of the SBC due to an increase in the sensible heat flux and increased low-level mixing. The model's inability to detect these subtle layers in

the observations is evident by the exaggerated expansion fan in the model that is associated with stronger winds further east into the SBC. Much higher resolution simulations might be able to pick up these layers, but at the present, such simulations are not feasible for operational use, and more so for any sort of long term study of mesoscale changes of wind stress near PAPC and the SBC.

The northerly component of the wind greatly impacts the MBL structure in the SBC. When strong offshore winds are simulated aloft in the SBC, the model greatly underestimates the height of the MBL. Strong offshore winds can happen. Parish et al. (2014) found that northerly winds with a clear continental origin contributed to the collapse of the MBL just to the east of Point Arguello. Northerly winds transport warm, dry air above the cool, moist MBL and enhances both the horizontal temperature gradient and the acceleration of the LLJ. The off-continent winds can be tied to the location of the MBL collapse, but for both RF01 and RF02, much stronger v-winds in the model greatly exaggerate the transition of the MBL and occur over a larger region. Therefore, the expansion fan extends much farther into the SBC. As observed, the lowest layer associated with the expansion fan near PAPC encounters a deeper, warmer layer that has an inversion aloft (Fig. 3.22 and 3.23). The original conceptual model in Dorman and Koračin (2008) made use of model data and concluded that the lowest layer deepens again as the flow moves eastward into the SBC, similar to what was found in WRF during RF02. However, the aircraft observations show the lowest layer simply dissipates towards the east instead of maintaining its identity and increasing its depth. Only the slightly warmer and deeper layer remains in the east of the SBC after the lowest layer with westerly flow dissipates.

An erroneous vertical structure also has large implications beyond simply understanding the fluid system or forecasting surface winds since it impacts atmospheric refractivity. This is especially important along the coast of California, where numerous national defense agencies use numerical weather prediction models for operational and tactical purposes. Implications arise due to the difficulty in accurately forecasting the refractivity index. These WRF simulations demonstrate that atmospheric ducting conditions are poorly modeled near PAPC and especially in the SBC. Because of the much stronger vertical gradient of temperature and humidity, WRF tends to overestimate an

elevated ducting layer in the SBC. In addition to much weaker vertical gradients, observations indicate there are a lot of fine-scale changes in temperature and humidity that lead to large variations of *M* (Fig. 3.27). Numerous small layers of large *M* changes lead to enhanced troposcatter, which would more quickly attenuate the signal. The strong stable inversion layer in the model would preclude troposcatter from being an issue, but ducting would be a major issue. The observations indicate that ducting in the SBC is not a major issue, but troposcatter could be an issue. If this atmospheric information is passed into EM propagation models, there would be two substantially different results.

REFERENCES

Atkinson, B. W., and M. Zhu, 2005: Radar-duct and boundary-layer characteristics over the area of the Gulf. *Quart. J. Roy. Meteor. Soc.*, **131**, 1923-1953.

Atkinson, B. W., and M. Zhu, 2006: Coastal effects on radar propagation in atmospheric ducting conditions. *Meteor. Appl.*, **13**, 53-62.

Basha, G., M. Venkat Ratnam, G. Manjula, and A. V. Chandra Sekhar, 2013: Anomalous propagation conditions observed over a tropical station using high-resolution GPS radiosonde observations. *Radio Sci*., **48**, 42-49.

Beardsley, R. C., C. E. Dorman, C. A. Friehe, L. K. Rosenfeld, and C. D. Winant, 1987: Local atmospheric forcing during the Coastal Ocean Dynamics Experiment: 1. A description of the marine boundary layer and atmospheric conditions over a northern California upwelling region. *J. Geophys*. *Res*., **92**, 1467-1488.

Boé, J., A. Hall, F. Colas, J. C. McWilliams, X. Qu, J. Kurian, and S. B. Kapnick, 2011: What shapes mesoscale wind anomalies in coastal upwelling zones? *Climate Dyn.*, **36**, 2037-2049.

Bravo, L., M. Ramos, O. Astudillo, B. Dewitte, and K. Goubanova, 2016: Seasonal variability of the Ekman transport and pumping in the upwelling system off central-northern Chile (~30° S) based on high-resolution atmospheric regional model (WRF). *Ocean Sci.*, **12**, 1049-1065.

Brooks, I. M., A. K. Goroch, and D. P. Rogers, 1999: Observations of strong surface radar ducts over the Persian Gulf. *J. Appl. Meteor*., **38**, 1293-1310.

Burk, S. D., T. Haack, and R. M. Samelson, 1999: Mesoscale simulation of supercritical, subcritical, and transcritical flow along coastal topography. *J. Atmos. Sci.*, **56**, 2780-2795.

Burk, S. D., and W. T. Thompson, 1996: The summertime low-level jet and marine boundary layer structure along the California coast. *Mon. Wea. Rev*., **124**, 668-686.

Burk, S. D., and W. T. Thompson, 1997: Mesoscale modeling of summertime refractive conditions in the southern California bight. *J. Appl. Meteor*., **36**, 22-31.

Capet, X. J., P. Marchesiello, and J. C. McWilliams, 2004: Upwelling response to coastal wind profiles. *Geophys. Res. Lett.*, **31**, L13311, doi:10.1029/2004GL020123.

Carvalho, D., A. Rocha, M. Gómez-Gesteira, and C. Santos, 2012: A sensitivity study of the WRF model in wind simulation for an area of high wind energy. *Environ. Modell. Softw.*, **33**, 23-34.

Carvalho, D., A. Rocha, M. Gómez-Gesteira, and C. Santos, 2014: Sensitivity of the WRF model wind simulation and wind energy production estimates to planetary boundary layer parameterizations for onshore and offshore areas in the Iberian Peninsula. *Appl. Energy.*, **135**, 234-246.

Chai, T., and R. R. Draxler, 2014: Root mean square error (RMSE) or mean absolute error (MAE)? – Arguments against avoiding RMSE in the literature. *Geosci. Model Dev.*, **7**, 1247-1250.

Chang, R., R. Zhu, M. Badger, C. B. Hasager, X. Xing, and Y. Jiang, 2015: Offshore wind resources assessment from multiple satellite data and WRF modeling over south China sea. *Remote Sens.*, **7**, 467-487.

Dorman, C. E., 1985: Evidence of kelvin waves in California's marine layer and related eddy generation. *Mon. Wea. Rev.*, **113**, 827-839.

Dorman, C. E., and D. Koračin, 2008: Response of the summer marine layer flow to an extreme California coastal bend. *Mon. Wea. Rev.*, **136**, 2894-2922.

Dorman, C. E., D. P. Rogers, W. Nuss, and W. T. Thompson, 1999: Adjustment of the summer marine boundary layer around Point Sur, California. *Mon. Wea. Rev.*, **127**, 2143-2159.

Dorman, C. E., and C. D. Winant, 2000: The structure and variability of the marine atmosphere around the Santa Barbara Channel. *Mon. Wea. Rev.*, **128**, 261-282.

Edinger, J. G., and M. G. Wurtele, 1972: Interpretation of some phenomena observed in southern California stratus. *Mon. Wea. Rev.*, **100**, 389-398.

Edwards, K. A., A. M. Rogerson, C. D. Winant, and D. P. Rogers, 2001: Adjustment of the marine atmospheric boundary layer to a coastal cape. *J. Atmos. Sci.*, **58**, 1511-1528.

Enriquez, A. G., and C. A. Friehe, 1996: Effects of wind stress and wind stress curl variability on coastal upwelling. *J. Phys. Oceanogr.*, **25**, 1651-1671.

Garreaud, R. D., J. A. Rutllant, R. C. Muñoz, D. A. Rahn, M. Ramos, and D. Figueroa, 2011: VOCALS-CUpEx: The Chilean Upwelling Experiment. *Atmos. Chem. Phys.*, **11**, 2015-2029.

Gerber, H., S. Chang, and T. Holt, 1989: Evolution of a marine boundary-layer jet. *J. Atmos. Sci.*, **46**, 1312-1326.

Haack, T., and S. D. Burk, 2001: Summertime marine refractivity conditions along coastal California. *J. Appl. Meteor.*, **40**, 673-687.

Haack, T., S. D. Burk, C. Dorman, and D. Rogers, 2001: Supercritical flow interaction within the Cape Blanco-Cape Mendocino orographic complex. *Mon. Wea. Rev.*, **129**, 688-708.

Haack, T., C. Wang, S. Garrett, A. Glazer, J. Mailhot, and R. Marshall, 2010: Mesoscale modeling of boundary layer refractivity and atmospheric ducting. *J. Appl. Meteor. Climatol*., **49**, 2437-2457.

Halliwell, G. R., Jr., and J. S. Allen, 1987: Wave-number frequency domain properties of coastal sea level response to alongshore wind stress along the west coast of North America (1980-1984). *J. Geophys. Res.*, **92**, 11761-11788.

Hsu, S. A., E. A. Meindl, and D. B. Gilhousen, 1994: Determining the power-law wind-profile exponent under near-neutral stability conditions at sea. *J. Appl. Meteor.*, **33**, 757-772.

Iacono, M. J., J. S. Delamere, E. J. Mlawer, M. W. Shephard, S. A. Clough, and W. D. Collins, 2008: Radiative forcing by long-lived greenhouse gases: Calculations with the AER radiative transfer models. *J. Geophys. Res.*, **113**, D13103, doi:10.1029/2008JD009944.

Janjic, Z. I., 1994: The step-mountain Eta coordinate model: Further developments of the convection, viscous sublayer and turbulence closure schemes. *Mon. Wea. Rev*., **122**, 927-945.

Jin, X., D. Changming, J. Kurian, J. C. McWilliams, D. B. Chelton, and Z. Li, 2009: SST-wind interaction in coastal upwelling: Oceanic simulation with empirical coupling. *J. Phys. Oceanogr.*, **39**, 2957-2970.

Koračin, D., and C. E. Dorman, 2001: Marine atmospheric boundary divergence and clouds along California in June 1996. *Mon. Wea. Rev*., **129**, 2040-2056.

Koračin, D., C. E. Dorman, and E. P. Dever, 2004: Coastal perturbations of marine-layer winds, wind stress, and wind stress curl along California and Baja California in June 1999. *J. Phys. Oceanogr.*, **34**, 1152-1173.

Koračin, D., J. Lewis, W. T. Thompson, C. E. Dorman, and J. A. Businger, 2001: Transition of stratus into fog along California coast: Observations and modeling. *J. Atmos. Sci.*, **58**, 1714-1731.

Lester, P. F., 1985: Studies of the marine inversion over the San Francisco Bay area... A summary of the work of Albert Miller, 1961-1978. *Bull. Amer. Meteor. Soc.*, **66**, 1396-1402.

Mass, C. F., J. Baars, G. Wedam, E. Grimit, and R. Steed, 2008: Removal of systematic model bias on a model grid. *Wea. Forecasting*, **23**, 438-459.

Mattar, C., and D. Borvarán, 2016: Offshore wind power simulation by using WRF in the central coast of Chile. *Renew. Energy*, **94**, 22-31.

Melton, C., L. Washburn, and C. Gotschalk, 2009: Wind relaxations and poleward flow events in a coastal upwelling system on the central California coast. *J. Geophys. Res.*, **114**, C11016, doi:10.1029/2009JC005397.

Morrison, H., G. Thompson, and V. Tatarskii, 2009: Impact of cloud microphysics on the development of trailing stratiform precipitation in a simulated squall line: Comparison of one- and two-moment schemes. *Mon. Wea. Rev.*, **137**, 991-1007.

Parish, T. R., 2000: Forcing of the summertime low-level jet along the California coast. *J. Appl. Meteor.*, **39**, 2421-2433.

Parish, T. R., D. A. Rahn, and D. Leon, 2014: Aircraft observations of the marine boundary layer adjustment near Point Arguello, California. *J. Appl. Meteor. Climatol*., **53**, 970-988.

Parish, T. R., D. A. Rahn, and D. Leon, 2015: Aircraft observations and numerical simulations of the developing stage of a southerly surge near southern California. *Mon. Wea. Rev.*, **143**, 4883-4903.

Parish, T. R., D. A. Rahn, and D. Leon, 2016a: Research aircraft determination of D-value cross-sections. *J. Atmos. Oceanic Technol.*, **33**, 391-396.

Parish, T. R., D. A. Rahn, and D. Leon, 2016b: Aircraft measurements and numerical simulations of an expansion fan off the California coast. *J. Appl. Meteor. Climatol*., **55**, 2053-2062.

Perlin, N., E. D. Skyllingstad, and R. M. Samelson, 2011: Coastal atmospheric circulation around an idealized cape during wind-driven upwelling studied from a coupled ocean-atmosphere model. *Mon. Wea. Rev.*, **139**, 809-829.

Pickett, M. H., and J. D. Paduan, 2003: Ekman transport and pumping in the California current based on the U.S. Navy's high-resolution atmospheric model (COAMPS). *J. Geophys. Res*., **108**, 1978-2012.

Pomeroy, K. R., and T. R. Parish, 2001: A case study of the interaction of the summertime coastal jet with the California topography. *Mon. Wea. Rev.*, **129**, 530-539.

Rahn, D. A., T. R. Parish, and D. Leon, 2013: Airborne measurements of coastal jet transition around Point Conception, California. *Mon. Wea. Rev.*, **141**, 3827-3839.

Rahn, D. A., T. R. Parish, and D. Leon, 2014: Coastal jet adjustment near Point Conception, California, with opposing wind in the bight. *Mon. Wea. Rev.*, **142**, 1344-1360.

Rahn, D. A., T. R. Parish, and D. Leon, 2016: Observations of large wind shear above the marine boundary layer near Point Buchon, California. *J. Atmos. Sci.*, **73**, 3059-3077.

Ranjha, R., M. Tjernström, G. Svensson, and A. Semedo, 2016: Modelling coastal low-level wind-jets: does horizontal resolution matter? *Meteor. Atmos. Phys.*, **128**, 128-263.

Renault, L., B. Dewitte, M. Falvey, R. Garreaud, V. Echevin, and B. Fabrice, 2009: Impact of atmospheric coastal jet off central Chile on sea surface temperature from satellite observations (2000-2007). *J. Geophys. Res.*, **114**, C08006, doi:10.1029/2008JC005083.

Renault, L., and Coauthors, 2012: Upwelling response to atmospheric coastal jets off central Chile: A modeling study of the October 2000 event. *J. Geophys. Res.*, **117**, C02030, doi:10.1029/2011JC007446.

Rogers, D. P., and Coauthors, 1998: Highlights of Coastal Waves 1996. *Bull. Amer. Meteor. Soc.*, **79**, 1307-1326.

Rogerson, A. M., 1999: Transcritical flows in the coastal marine atmospheric boundary layer. *J. Atmos. Sci.*, **56**, 2761-2779.

Seo, H., K. Brink H., C. E. Dorman, and D. Koračin, 2012: What determines the spatial pattern in summer upwelling trends on the U.S. west coast? *J. Geophys. Res.*, **117**, 1978-2012.

Shimada, S., and T. Ohsawa, 2011: Accuracy and characteristics of offshore wind speeds simulated by WRF. *SOLA*, **7**, 21-24.

Skamarock, W. C., and Coauthors, 2008: A description of the Advanced Research WRF version 3. NCAR Tech. Note NCAR/TN-475+STR, 113 pp, doi:10.5065/D68S4MVH.

Skyllingstad, E. D., P. Barbour, and C. E. Dorman, 2001: The Dynamics of Northwest Summer Winds over the Santa Barbara Channel. *Mon. Wea. Rev.*, **129**, 1042-1061.

Tewari, M., and Coauthors, 2004: Implementation and verification of the unified NOAH land surface model in the WRF model. *20th Conf. on weather analysis and forecasting/16th Conf. on numerical weather prediction*, Seattle, WA, Amer. Meteor. Soc., 14.2a. [Available online at https://ams.confex.com/ams/84Annual/techprogram/paper_69061.htm].

Thompson, W. T., and T. Haack, 2011: An investigation of sea surface temperature influence on microwave refractivity: The Wallops-2000 Experiment. *J. Appl. Meteor. Climatol.*, **50**, 2319-2337.

Wang, C., D. Wilson, T. Haack, P. Clark, H. Lean, and R. Marshall, 2012: Effects of initial and boundary conditions of mesoscale models on simulated atmospheric refractivity. *J. Appl. Meteor. Climatol.*, **51**, 115-132.

Washburn, L., M. R. Fewings, C. Melton, and C. Gotschalk, 2011: The propagating response of coastal circulation due to wind relaxations along the central California coast, *J. Geophys. Res.*, **116**, C12028, doi:10.1029/2011JC007502.

Washburn, L., and E. McPhee-Shaw, 2013: Coastal transport processes affecting inner-shelf ecosystems in the California current system. *Oceanography*, **26**, 34-43.

Winant, C. D., C. E. Dorman, C. A. Friehe, and R. C. Beardsley, 1988: The marine boundary layer off northern California: An example of supercritical channel flow. *J. Atmos. Sci.*, **45**, 3588-3605.

Zhao, Q., T. Haack, J. McLay, and C. Reynolds, 2016: Ensemble prediction of atmospheric refractivity conditions for EM propagation. *J. Appl. Meteor. Climatol.*, **55**, 2113-2130.

APPENDIX

Supplementary Tables

Table A1: The WRF namelist for the WRF Preprocessing System (WPS). Three main programs (geogrid, ungrib, and metgrid) prepare the input for real-data simulations. Detailed information regarding each programs functionality and description of namelist variables can be found in chapter 3 of the WRF user guide available online at http://www2.mmm.ucar.edu/wrf/users/docs/user_guide_V3/users_guide_chap3.htm.

```
&share
 wrf_core = 'ARW',
 start_date = '2012-05-18_00:00:00','2012-05-18_00:00:00',
 end_date   = '2012-05-20_00:00:00','2012-05-20_00:00:00',
 interval_seconds = 21600,
 io_form_geogrid = 2,
&geogrid
 parent_id         = 1, 1,
 parent_grid_ratio = 1, 3,
 i_parent_start    = 1, 106,
 j_parent_start    = 1, 40,
 e_we              = 202, 196,
 e_sn              = 193, 199,
 geog_data_res     = '30s', '30s',
 dx = 9000,
 dy = 9000,
 map_proj = 'lambert',
 ref_lat   = 37.0,
 ref_lon   = -124.0,
 truelat1  = 25.0,
 truelat2  = 45.0,
 stand_lon = -124.0,
 geog_data_path = '/scratch/c804m051/geog/',
&ungrib
 out_format = 'WPS',
 prefix = 'FILE',
&metgrid
 fg_name = 'FILE',
 io_form_metgrid = 2,
```

Table A2: The WRF namelist for the model initialization and numerical integration programs. Detailed information regarding the description of namelist variables and physics and dynamics options can be found in chapter 5 of the WRF user guide available online at http://www2.mmm.ucar.edu/wrf/users/docs/user_guide_V3/users_guide_chap5.htm

```
&time_control
 run_hours                  = 48,
 start year                 = 2012,  2012,
 start_month                = 05,    05,
 start_day                  = 18,    18,
 start_hour                 = 00,    00,
 start_minute               = 00,    00,
 start_second               = 00,    00,
 end_year                   = 2012,  2012,
 end_month                  = 05,    05,
 end_day                    = 20,    20,
 end_hour                   = 00,    00,
 end_minute                 = 00,    00,
 end_second                 = 00,    00,
 interval_seconds           = 21600,
 input_from_file            = .true.,.true.,
 history_interval           = 60,    60,
 frames_per_outfile         = 1000,  1000,
 restart                    = .false.,
 restart_interval           = 720,
 io_form_history            = 2,
 io_form_restart            = 2,
 io_form_input              = 2,
 io_form_boundary           = 2,
 debug_level                = 0,
&domains
 time_step                  = 30,
 time_step_fract_num        = 0,
 time_step_fract_den        = 1,
 max_dom                    = 2,
 e_we                       = 202,   196,
 e_sn                       = 193,   199,
 e_vert                     = 84,    84,
 p_top_requested            = 10000,
 num_metgrid_levels         = 40,
 num_metgrid_soil_levels    = 4,
 dx                         = 9000,  3000,
 dy                         = 9000,  3000,
 grid_id                    = 1,     2,
 parent_id                  = 1,     1,
 i_parent_start             = 1,     106,
```

```
 j_parent_start           = 1,     40,
 parent_grid_ratio        = 1,     3,
 parent_time_step_ratio   = 1,     3,
 feedback                 = 1,
 smooth_option            = 0,
&physics
 mp_physics               = 10,    10,
 ra_lw_physics            = 4,     4,
 ra_sw_physics            = 4,     4,
 radt                     = 3,     3,
 sf_sfclay_physics        = 2,     2,
 sf_surface_physics       = 2,     2,
 bl_pbl_physics           = 2,     2,
 bldt                     = 0,     0,
 cu_physics               = 2,     2,
 cudt                     = 0,     0,
 isfflx                   = 1,
 ifsnow                   = 1,
 icloud                   = 1,
 surface_input_source     = 1,
 num_soil_layers          = 4,
 sf_urban_physics         = 0,     0,
&fdda
&dynamics
 w_damping                = 0,
 diff_opt                 = 1,     1,
 km_opt                   = 4,     4,
 diff_6th_opt             = 0,     0,
 diff_6th_factor          = 0.12,  0.12,
 base_temp                = 290.,
 damp_opt                 = 0,
 zdamp                    = 5000., 5000.,
 dampcoef                 = 0.2,   0.2,
 khdif                    = 0,     0,
 kvdif                    = 0,     0,
 non_hydrostatic          = .true.,.true.,
 moist_adv_opt            = 1,     1,
 scalar_adv_opt           = 1,     1,
&bdy_control
 spec_bdy_width           = 5,
 spec_zone                = 1,
 relax_zone               = 4,
 specified                = .true.,.false.,
 nested                   = .false.,.true.,
&grib2
&namelist_quilt
 nio_tasks_per_group      = 0,
 nio_groups               = 1,
```

Table A3: The daily synoptic forcing metric during May and June 2012. The daily mean wind speed U at several buoys and the diurnal range $U_{range} = (U_{max} - U_{min})$ are calculated to characterized each day as a strong, moderate or weak event. The thresholds for the forcing criteria are listed at the top of the table.

May and June 2012 Daily Synoptic Forcing Metric		
Strong Event	Moderate Event	Weak Event
▪ $U \geq 11$ m s^{-1} at b-42	▪ $5 < U < 11$ m s^{-1} at b-42	▪ $U \leq 5$ m s^{-1} at b-42
▪ $U \geq 11$ m s^{-1} at b-28	▪ $5 < U < 11$ m s^{-1} at b-28	▪ $U \leq 5$ m s^{-1} at b-28
▪ $U \geq 11$ m s^{-1} at b-54	▪ $5 < U < 11$ m s^{-1} at b-54	▪ $U \leq 5$ m s^{-1} at b-54
▪ $U_{range} < 4$ m s^{-1} at b-54	▪ $U_{range} \geq 4$ m s^{-1} at b-54	▪ U at b-53 > U at any one or more buoys
▪ $U_{min} \geq 7$ m s^{-1} at b-54	▪ $U_{min} < 7$ m s^{-1} at b-54	▪ $U_{max} < 7$ m s^{-1} at b-54

Date	U b-42	U b-28	U b-54	U b-53	U_{max} b-54	U_{min} b-54	U_{range} b-54	Synoptic Forcing		
								Strong	Mod.	Weak
May 1	10.9	11.7	7.3	4.3	10.8	1.0	9.8		*	
2	8.4	10.2	9.4	3.9	11.1	7.3	3.8		*	
3	3.7	4.1	9.4	4.5	10.4	8.1	2.3			*
4	9.7	11.2	11.6	4.0	14.8	8.4	6.4	*		
5	10.8	11.6	12.2	3.1	14.3	9.9	4.4	*		
6	9.2	8.6	6.8	2.4	10.9	0.7	10.2		*	
7	8.0	8.2	5.6	5.0	12.4	0.4	12.0		*	
8	7.2	7.8	10.6	7.1	12.4	8.0	4.4		*	
9	9.4	10.7	10.8	6.3	13.1	7.3	5.8		*	
10	7.8	9.3	8.8	5.3	13.3	5.9	7.4		*	
11	2.8	2.4	3.2	3.6	6.5	1.0	5.5			*
12	2.9	2.2	3.0	3.7	7.0	0.2	6.8			*
13	3.7	2.1	7.7	6.3	10.4	4.8	5.6			*
14	3.9	3.9	8.3	9.0	9.8	5.1	4.7			*
15	6.6	9.8	11.4	4.3	14.9	8.1	6.8		*	
16	8.1	10.6	13.8	5.5	15.3	12.9	2.4	*		
17	8.2	11.7	12.7	7.3	15.2	8.8	6.4	*		

18	10.0	12.0	12.0	5.6	14.3	10.2	4.1	*		
19	9.0	11.3	10.3	3.1	12.1	8.1	4.0		*	
20	9.2	11.5	7.7	3.3	13.5	1.4	12.1		*	
21	7.1	12.1	13.4	4.4	14.8	11.5	3.3	*		
22	8.0	12.9	14.1	2.5	16.2	11.7	4.5	*		
23	12.5	14.4	14.6	10.3	15.9	13.4	2.5	*		
24	11.9	14.0	14.4	2.6	15.6	12.9	2.7	*		
25	10.8	8.7	10.9	9.8	13.8	8.1	5.7		*	
26	7.5	8.2	8.9	9.7	10.0	6.3	3.7		*	
27	6.8	10.1	11.3	4.5	13.1	8.2	4.9		*	
28	7.5	11.5	11.4	3.6	13.8	8.6	5.2	*		
29	8.8	11.0	13.1	5.1	14.5	12.2	2.3	*		
30	8.7	10.4	12.5	4.1	14.2	11.6	2.6	*		
31	7.6	10.3	11.8	3.7	13.6	9.1	4.5		*	
June 1	9.3	10.1	9.2	4.7	13.4	1.5	11.9		*	
2	5.6	11.4	10.3	2.5	12.9	3.7	9.2		*	
3	6.2	9.7	9.2	3.6	12.3	6.6	5.7		*	
4	3.4	5.9	8.1	5.2	12.0	3.9	8.1		*	
5	7.5	10.4	13.7	11.8	15.2	11.8	3.4	*		
6	10.2	13.2	14.4	7.8	15.6	13.3	2.3	*		
7	7.8	13.6	13.3	2.7	16.4	5.5	10.9		*	
8	9.6	14.2	11.9	2.2	14.8	8.1	6.7	*		
9	11.7	13.4	11.4	2.7	15.7	6.7	9.0	*		
10	6.9	5.4	3.6	3.0	8.3	1.1	7.2		*	
11	7.5	3.5	4.6	2.9	8.5	2.1	6.4		*	
12	8.8	10.0	5.8	3.2	12.8	0.4	12.4		*	
13	8.9	10.0	11.5	5.2	13.5	10.0	3.5	*		
14	8.7	8.5	9.2	4.6	10.7	7.5	3.2		*	
15	7.2	6.9	6.2	3.5	10.9	0.3	10.6		*	
16	3.2	2.6	3.2	3.5	5.3	1.1	4.2			*
17	4.1	5.1	3.3	3.5	7.0	0.4	6.6			*
18	3.7	2.7	8.1	7.2	10.7	5.7	5.0			*
19	3.9	3.6	9.4	6.8	11.9	6.7	5.2			*

20	6.6	5.3	7.0	4.9	9.7	4.1	5.6		*	
21	5.3	7.0	9.9	5.7	12.6	7.2	5.4		*	
22	3.5	6.5	11.7	6.2	13.6	8.7	4.9		*	
23	5.8	7.7	11.1	5.2	13.1	8.6	4.5		*	
24	4.7	7.6	10.1	5.3	11.2	8.7	2.5		*	
25	3.5	6.5	9.6	5.5	11.2	8.6	2.6		*	
26	8.8	10.1	10.5	4.2	11.1	9.6	1.5		*	
27	9.7	10.0	7.8	4.5	10.3	0.7	9.6		*	
28	8.6	8.8	9.4	4.8	11.8	6.9	4.9		*	
29	6.5	8.8	11.8	4.2	12.8	10.3	2.5	*		
30	4.8	7.5	12.0	4.8	13.6	9.7	3.9	*		